Estimation of geological dip and curvature from time-migrated zero-offset reflections in heterogeneous anisotropic media

Martin Tygel[*], Bjørn Ursin[†], Einar Iversen [‡], and Maarten V. de Hoop[§]

[*]*State University of Campinas (UNICAMP),*

Applied Mathematics Department, IMECC,

CP 6065, Campinas SP, Brazil

[†]*Norwegian University of Science and Technology (NTNU),*

Department of Petroleum Engineering and Applied Geophysics,

S.P. Andersensvei 15A, NO-7491 Trondheim, Norway

[‡]*NORSAR, P.O. Box 53, 2027 Kjeller, Norway*

[§]*Center for Computational and Applied Mathematics, Purdue University,*

150 N. University Street, West Lafayette IN 47907, USA

(September 20, 2010)

Running head: **Estimation of geological dip and curvature**

ABSTRACT

Starting from a given time-migrated section and time migrated velocity field, recent literature has shown that it is possible to simultaneously trace image rays in depth and reconstruct the depth-velocity model along them. This, in turn, allows image-ray migration, namely to map time-migrated horizons into depth by moving the horizon time samples along the image

ray until half the traveltime is consumed. As known since the 1980s, image-ray migration can be made more complete if, besides traveltime, also estimations of its first and second derivatives with respect to lateral image coordinates are available. Such additional information, provides, in addition to the location of the reflectors in depth, also an estimation of their geological dip and curvature. The expressions explicitly relate geological dip and curvature to first and second derivatives with respect to image coordinates of time-migrated reflection surfaces. The latter can be estimated directly from the time-migrated volume, for example by use of the common-reflection-surface method. Such quantitative relationships can provide useful constraints for construction of selected reflectors at depth. So far, image-ray migration algorithms are restricted to layered models with isotropic, smooth velocity distributions within the layers. Using the attractive methodology of surface-to-surface propagator matrices, we obtain a natural extension of image-ray migration to smooth or layered anisotropic media. Numerical examples illustrate the procedure.

INTRODUCTION

Time migration, either post-stack or pre-stack, is widespread used in seismic processing to produce initial time-domain images and velocity in a simple and efficient way (Hubral and Krey, 1980; Yilmaz, 2000). Together with its advantages of computational efficiency and robustness with respect to a background velocity model, time migration has the the drawback of producing distorted images, in some cases, even under mild lateral velocity variations (Robein, 2003). An option to correct lateral positioning errors of time migration is to convert the time-migrated images into depth, which includes, as an obligatory step, the conversion of the time-migrated velocities into a corresponding depth-velocity field.

The theoretical explanation of the time migration procedure has been given in Hubral (1977) by means of the concept of image rays. For an isotropic medium, the image ray starts normally to the measurement (time-migration datum) surface and travels down to hit, generally non-normally, the reflector. In this way, it can be seen as a "dual" of a normal ray, which starts, generally non-normally, at the measurement (acquisition datum) surface and hits normally the reflector. For an anisotropic medium, the duality between the image and normal rays is still valid: in this case, it is not the ray but the slowness vector that is normal to the measurement surface (image ray) and the reflector (normal ray).

A better insight on the advantages and limitations on the time-migration process can be gained by simple numerical simulations. In Figure 1 we show normal- and image-ray fields for a syncline-shape reflector situated in a homogeneous and isotropic depth velocity field. The measurement surface under consideration is a horizontal plane. The normal-ray trajectories in Figure 1(a) are perpendicular to the reflector, whereas the the image-ray trajectories in Figure 1(b) are perpendicular to the measurement surface. The corresponding

3

two-way time responses, see Figure 2, yield a triplication in the unmigrated time domain and a single-valued, non-distorted, reflector image in the migrated time domain. Introducing now a low-velocity inclusion between the syncline and the measurement surface (Figure 3), the normal- and image ray fields change dramatically in complexity. Both ray fields exhibit triplications and caustics, as a result of the low velocity anomaly. However, these effects show up differently in the unmigrated and migrated time domains, see Figure 4. In the unmigrated time domain the reflector traveltime is clearly multi-valued, while this is not the case in the migrated time domain. However, in spite of its single-valuedness it is no doubt that the migrated reflection traveltime in Figure 4(b) yields a highly unsatisfactory image of the reflector. In fact, the introduction of a caustic in the image-ray field implies that there is no longer a one-to-one correspondence between points in the depth domain and the migrated time domain, and migration velocities related to the caustic become infinite. Caustics and triplications in the image-ray field are therefore incompatible with the basic assumptions inherent to seismic time migration. As a consequence, it is mandatory to smooth migration velocities as well as corresponding depth velocities, so to ensure that the mentioned one-to-one correspondence between the domains is not violated.

Quite recently, Cameron et al. (2006, 2007) unveiled the theoretical relationship between the time-migrated and depth velocity fields and presented algorithms to estimate depth velocities and trace image rays from a given time-migrated velocity field. A modified algorithm for the same purposes has been also presented in Iversen and Tygel (2008). Application of the theory to actual time-to-depth conversion has been presented in Cameron et al. (2008). The above papers show that an isotropic depth velocity field and also image rays can be fully constructed from a given time-migrated velocity field. As a consequence, individual time-migrated reflection curves can be readily converted into depth by simply

moving time samples along the image ray.

As well recognized in the seismic literature, more detailed images and velocity information can be gained if, not only traveltimes, but also slopes and curvatures (e.g., first and second derivatives of traveltime with respect to measurement coordinates) are estimated from the data. Examples in this direction include, among others, plane-wave destructors (Claerbout, 1992; Fomel, 2002), time-domain seismic imaging using local event slopes (Fomel, 2007), the common-reflection-surface (CRS) stacking method (Hertweck et al., 2004) and the multifocus (MF) stacking method (Landa et al., 1999), as well as macro-velocity model building by the methods of stereotomography (Bilette and Lambaré, 1998) and NIP-wave tomography (Iversen and Gjøystdal, 1984; Duveneck, 2004).

In unmigrated stacked data, non-converted reflections or, more generally, symmetric reflections*, admit a well-known interpretation for their first and second derivatives of traveltime with respect to source-receiver common midpoint (CMP) coordinates. Following general ray theoretical principles, a stacked reflection event (horizon) can be seen as the response of a specific (target) reflector under illumination of normal-incidence rays with specific wavemode (Hubral and Krey, 1980). Each of these rays has starting and ending points coinciding with a CMP. Moreover, at the point where the ray hits the target reflector, called the normal-incidence-point (NIP), the slowness vector is normal to the reflector. With the above understanding, on an observed symmetric reflection horizon, we have for each CMP:

(a) The observed horizon time coincides with the traveltime of the normal-incidence ray

---

*For a given target reflector, an elementary reflection such that its ray code from the source to the reflector coincides with the ray code of the ray from the reflector to the receiver in reverse order is referred to as a symmetric reflection. For more details, the reader is referred to Tygel and Santos (2007).

5

corresponding to that given CMP.

(b) The first-derivatives (slopes) of the observed horizon time with respect to midpoint coordinates equal the two horizontal slownesses of the normal-incidence ray at the given CMP. If the near-surface velocity is known, one can convert the slownesses into the corresponding emergence and azimuth angles of the normal-incidence ray.

(c) The second derivatives of the observed horizon time with respect to midpoint coordinates are proportional to the wavefront curvature, measured at the given CMP, of the so-called normal (N) wave associated with the normal-incidence ray which travels along the normal-incidence ray (Hubral, 1983; Iversen, 2006).

Following Hubral (1983), the N-wave is a fictitious *eigenwave* which propagates along the normal-incidence ray and is such that it has coinciding wavefronts at its starting and endpoints. Moreover, the N-wave is characterized by the property that its wavefront coincides with the shape of the target reflector in the vicinity of the point NIP. The (two-way) N-wave in Hubral (1983) has been modified by Iversen (2006) to designate the also fictitious (one-way) wave that starts at the reflector with a wavefront coinciding with the shape of the target reflector in the vicinity of the point NIP and propagates upward. The N-waves of Hubral (1983) and Iversen (2006) have the same wavefront curvature at the CMP.

The above considerations imply that, if a depth velocity model is available, one can depth convert an observed stacked, symmetric, primary reflection as follows: For each CMP:

(i) Use the emergence and azimuth angles provided by the traveltime slopes to trace the normal-incidence ray back into depth. The NIP point at the reflector is reached when half the traveltime is consumed.

(ii) Propagate the wavefront curvature of the N-wave, provided by the second-derivatives of traveltime, along the normal-incidence ray into depth. The wavefront curvature at the the point NIP equals the curvature of the target reflector at that point.

Referred to as *map migration* or *normal ray migration*, the above algorithm has been formulated and applied for a given depth model of homogeneous isotropic layers with curved interfaces (Kleyn, 1977; Hubral and Krey, 1980; Gjøystdal and Ursin, 1981; Ursin, 1982). For extensions allowing velocity gradients in the layers, see, e.g., Iversen and Gjøystdal (1984); Biloti et al. (2002). Although very attractive from the theoretical point of view, normal ray migration encounters serious problems to be implemented, because is high dependence on a complete velocity model and the difficulties (e.g., multipathing and triplications) in identifying (picking) reflections and their first and second derivatives in the unmigrated stacked data.

Based on the more friendly and robust properties of time-migrated reflections (e.g., collapse of diffractions, untangle of triplications, and less sensitivity of a macro-velocity model), a similar algorithm, referred to as *image ray migration* has been proposed by Hubral and Krey (1980). Also for a depth model of homogeneous isotropic layers with curved interfaces, the algorithm was able to depth propagate symmetric primary reflections in the time-migrated domain. Studies by Iversen, Åstebøl and Gjøystdal at NORSAR in the eighties (see Iversen et al., 1987, 1988) extend Hubral's algorithm to general isotropic depth-velocity models.

Here we use in the derivation the powerful machinery of surface-to-surface propagator matrices (see, e.g., Bortfeld, 1989; Červený, 2001) to suitably modify and extend the image ray migration algorithm to account for full anisotropy and inhomogeneity. The proposed

methodology is illustrated using synthetic data sets for a single-layered 2-D anisotropic model and a multi-layered 3-D isotropic model. Results obtained by these first and basic applications are very encouraging.

ZERO-OFFSET REFLECTIONS IN UNMIGRATED AND MIGRATED TIME DOMAIN

Routinely applied to unmigrated data, zero-offset stacking [e.g., by the common-midpoint (CMP) method] and pre-stack time migration are able to produce first, time-domain images of seismic data in a robust and efficient way. Stacking to zero offset transforms the unmigrated data, defined in terms of trace location (i.e., source-receiver midpoint and half-offset) and time, into a simulated zero-offset volume in terms of trace location (CMP coordinates) and zero-offset time. In the same way, pre-stack time migration and subsequent stacking to zero offset, transforms the unmigrated data into a time-migrated volume, defined by trace location [e.g., common-image-point (CIP) coordinates] and migrated time. More specifically, at least for primary events, ZO stacking (resp. pre-stack time migration) transforms unmigrated reflections of a target reflector into corresponding reflections of the same reflector under normal-incidence (respectively, image-ray) illumination.

In a sense, both procedures can be seen as data compression transformations from the five-dimensional unmigrated (record) domain into the three-dimensional ZO unmigrated or time-migrated domains.

From now on, we will restrict our attention to symmetric primary reflections of target reflectors after zero-offset stacking or pre-stack time migration. In the ZO-stacked domain, reflection traveltimes have the general form $T^X(\mathbf{x})$, where the coordinate vector $\mathbf{x} = (x_1, x_2)$

specifies the CMP (trace location) along the measurement surface, $\mathcal{X}$, in the unmigrated domain, i.e., the acquisition datum surface. It is common to approximate $T^X(\mathbf{x})$ to second order in $\mathbf{x}$, based on coefficients known at some reference location ($\mathbf{x} = \mathbf{x}_0$). In this respect, probably the most "natural" coefficients one can think of are the traveltime and its derivatives

$$T_0^X \ , \quad \mathbf{p}^X = \left(\frac{\partial T^X}{\partial x_I}\right) \ , \quad \text{and} \quad \mathbf{M}^X = \left(\frac{\partial^2 T^X}{\partial x_I \partial x_J}\right) \ , \tag{1}$$

evaluated at $\mathbf{x} = \mathbf{x}_0$ and with indices I, J taking the values 1 or 2. These coefficients can be computed directly from the seismic prestack data, without knowledge of the depth-velocity model.

In the time-migrated domain, reflections have the similar form, $T^M(\mathbf{m})$, where vector $\mathbf{m} = (m_1, m_2)$ specifies the CIP (trace location) along the time-migration datum surface. The latter is our measurement surface, $\mathcal{M}$, in the time-migrated domain. The traveltime parameters corresponding to those in equations 1 are

$$T_0^M \ , \quad \mathbf{p}^M = \left(\frac{\partial T^M}{\partial m_I}\right) \ , \quad \text{and} \quad \mathbf{M}^M = \left(\frac{\partial^2 T^M}{\partial m_I \partial m_J}\right) \ , \tag{2}$$

all of these functions evaluated at $\mathbf{m} = \mathbf{m}_0$. Throughout this paper the time T_0^M as well as the linear (slope) and and quadratic (curvature) parameters $\mathbf{p}^M$ and $\mathbf{M}^M$ in equations 2 are considered as measured quantities. Moreover, to simplify the notation, we set the coordinate systems, both in the unmigrated and migrated domains, such that their origins are situated at the respective reference points. In other words, we have $\mathbf{x}_0 = \mathbf{m}_0 = \mathbf{0}$.

Parabolic reflection traveltime in the unmigrated domain

In the following, we find it convenient to consider *parabolic* approximations of traveltime instead of the usual *hyperbolic* approximations. There is no lack of generality in doing so,

and moreover, the obtained results are the same for the two approximations. For a specified horizon (target reflection), we consider the reflection traveltimes, $T^X(\mathbf{x})$, in the vicinity of a selected trace location (reference point), $\mathbf{x}_0$, are well approximated by a Taylor parabolic polynomial of the form

$$T^X(\mathbf{x}) = T_0^X + \mathbf{x}^T\mathbf{p}^X + \frac{1}{2}\mathbf{x}^T\mathbf{M}^X\mathbf{x} \ . \tag{3}$$

Here, T_0^X, $\mathbf{p}^X$ and $\mathbf{M}^X$ are, respectively, the traveltime and its linear (first-derivative vector) and quadratic (second-derivative matrix) coefficients, as given by equation 1 with $\mathbf{x}_0 = \mathbf{0}$.

Parabolic reflection traveltime in time-migrated domain

As previously indicated, we denote by $\mathbf{m}$ the coordinate vectors that locate the zero-offset traces in the time-migrated domain. In the same way, we consider the Taylor parabolic approximation of the time-migrated reflection traveltime of a target reflector, $T^M(\mathbf{m})$, at trace location, $\mathbf{m}$, in the vicinity of a reference trace at the origin $\mathbf{m}_0 = \mathbf{0}$. It is given by

$$T^M(\mathbf{m}) = T_0^M + \mathbf{m}^T\mathbf{p}^M + \frac{1}{2}\mathbf{m}^T\mathbf{M}^M\mathbf{m} \ , \tag{4}$$

in which, the traveltime, T_0^M, and its linear and quadratic coefficients, $\mathbf{p}^M$ and $\mathbf{M}^M$, are given by equation 2 with $\mathbf{m}_0 = \mathbf{0}$. For the typical situation of a symmetric time migrated primary reflection, the above expression can be interpreted as twice the traveltime along the *image ray* from the initial point with coordinate $\mathbf{m}$ to the point where it hits the target reflector. The time T_0^M is twice the traveltime along the image ray from the reference point to the *image incident point (IIP)*, namely the point where this image ray hits the reflector.

It is our aim to characterize the geometric attributes, namely dip and curvature of the reflector at the point IIP in depth, as functions of the coefficients $\mathbf{p}^M$ and $\mathbf{M}^M$.

FORMULATION

The formulation of our problem requires an adequate selection of coordinates. Here, we will consider, besides coordinates at the measurement and target reflector surfaces, also auxiliary, so-called *wavefront* coordinates.

Measurement and reflector coordinates

Referring to Figure 5, points on the time-migration measurement (datum) surface, $\mathcal{M}$, and the target reflector, $\mathcal{Z}$, in the vicinity of the initial and endpoints of a selected reference (central) image ray will be specified by local 3-D Cartesian systems, $\hat{\mathbf{m}} = (m_1, m_2, m_3) = (\mathbf{m}, m_3)$ and $\hat{\mathbf{z}} = (z_1, z_2, z_3) = (\mathbf{z}, z_3)$. These systems will be referred to as *measurement* and *reflector* coordinate systems, respectively. Figure 5(a) depicts a general scenario including a curved measurement surface. For time migration it is common to take this surface as planar and horizontal [Figure 5(b)] in order to avoid surface-induced image distortions. Nevertheless, the situation in Figure 5(a) is of interest, as we derive fundamental relations in surface-to-surface propagation (Appendix A) with applications in a more general context.

The $\hat{\mathbf{m}}$-system has its origin at the initial point, $O^{\mathcal{M}} = \text{CIP}$, of the central image ray and the m_3-axis points in the direction of the surface normal to $\mathcal{M}$ at $O^{\mathcal{M}}$. Moreover, the m_1- and m_2 axes are orthogonal and lie at the plane, $\Pi^{\mathcal{M}}$, tangent to $\mathcal{M}$ at $O^{\mathcal{M}}$. The orientations of the axes m_1 and m_2 are unique only up to a rotation around the m_3-axis.

In an analogous way, the $\hat{\mathbf{z}}$-system has its origin at the endpoint, $O^{\mathcal{Z}} = \text{IIP}$, of the central image ray and its axis z_3 points in the direction of the normal of $\mathcal{Z}$ at $O^{\mathcal{Z}}$. The remaining (z_1- and z_2-) axes lie on the plane, $\Pi^{\mathcal{Z}}$, tangent to $\mathcal{Z}$ at $O^{\mathcal{Z}}$. The actual locations of the axes z_1 and z_2 are unique up to an arbitrary rotation about the reflector normal (z_3-axis).

In local Cartesian reflector coordinates, the reflector is assumed in the form

$$z_3 = \Sigma^{\mathcal{Z}}(\mathbf{z}) \ , \tag{5}$$

with the properties

$$\Sigma^{\mathcal{Z}}(\mathbf{0}) = 0, \quad \frac{\partial \Sigma^{\mathcal{Z}}}{\partial \mathbf{z}}(\mathbf{0}) = \mathbf{0} \ , \quad \text{and} \quad \frac{\partial^2 \Sigma^{\mathcal{Z}}}{\partial \mathbf{z}^2}(\mathbf{0}) = -\mathbf{D} \ , \tag{6}$$

where $\mathbf{D}$ is the reflector curvature matrix. The two left-most equations above incorporate the fact that the reflector is tangent to the $\mathbf{z}$-axis at the origin, $O^{\mathcal{Z}}$.

We observe that, although the system $\hat{\mathbf{m}}$ can be readily constructed on the (known) measurement surface, this is not the case for the $\hat{\mathbf{z}}$-system, constructed on the (unknown) reflector. As seen below, the $\hat{\mathbf{z}}$ system (together with the reflector dip at $O^{\mathcal{Z}}$=IIP), will be determined from the knowledge of T_0^M, $\mathbf{p}^M$. The reflector curvature at the IIP will additionally require the matrix $\mathbf{M}^M$.

The wavefront coordinate system

As indicated above, we assume that a depth-velocity model is known. As a consequence, the central image ray can be traced into depth, so that the point where it hits the reflector, namely the IIP, can also be assumed as known. The point IIP, which coincides with the origin of the $\hat{\mathbf{z}}$-system, is obtained by following the central image ray trajectory until the time $t = T_0^M/2$ is consumed. Moreover, the slowness vector, $\hat{\mathbf{p}}$, is normal to the wavefront at the IIP, namely,

$$\hat{\mathbf{p}} = \frac{1}{c}\hat{\mathbf{n}} \ , \tag{7}$$

where $\hat{\mathbf{n}}$ denotes the wavefront unit normal and c is the phase velocity. Quantities belonging to the wavefront-orthonormal coordinate system will be denoted with a superscript Y.

Figure 5 depicts both the $\hat{\mathbf{z}}$-reflector and the $\hat{\mathbf{y}}$-orthonormal wavefront coordinate systems with origin at the IIP.

Considering wavefront-orthonormal coordinates, the slowness and ray-velocity vectors are written

$$\hat{\mathbf{p}}^Y = \begin{pmatrix} \mathbf{0} \\ 1/c \end{pmatrix}, \qquad \hat{\mathbf{v}}^Y = \begin{pmatrix} \mathbf{v}^Y \\ c \end{pmatrix}. \tag{8}$$

Moreover, the vector $\mathbf{v}^Y$ is zero if the medium is isotropic at the actual IIP.

RELATING WAVEFRONT AND REFLECTOR COORDINATES

Following Červený (2001) the transformation from local wavefront-orthonormal to local reflector-orthonormal coordinates is described to the first order by the relation

$$\hat{\mathbf{z}} = \hat{\mathbf{G}}\hat{\mathbf{y}} . \tag{9}$$

Being a coordinate transformation between Cartesian coordinate systems, matrix $\hat{\mathbf{G}}$ is an orthonormal rotation matrix. As such, it satisfies the relation

$$\hat{\mathbf{G}}^{-1} = \hat{\mathbf{G}}^T . \tag{10}$$

Matrix $\hat{\mathbf{G}}$ has as columns the unit vectors of the wavefront-orthonormal coordinate system expressed with respect to the reflector coordinate system. The third column of matrix $\hat{\mathbf{G}}$ is therefore a unit vector normal to the wavefront in $\hat{\mathbf{z}}$-coordinates. That vector is denoted by $\hat{\mathbf{n}}^Z = (n_1^Z, n_2^Z, n_3^Z) = (\mathbf{n}^Z, n_3^Z)$, where the superscript Z signifies that the vector belongs to the reflector coordinate system.

In the same way, the orthonormality of matrix $\hat{\mathbf{G}}$ (equation 10), implies that the third line of that matrix is given by the transpose of the unit vector normal to the reflector, expressed in $\hat{\mathbf{y}}$-coordinates, namely $\hat{\boldsymbol{\nu}}^Y = (\nu_1^Y, \nu_2^Y, \nu_3^Y) = (\boldsymbol{\nu}^Y, \nu_3^Y)$. Vector $\hat{\boldsymbol{\nu}}$ is very important

as it defines the reflector dip. Note especially that

$$\nu_3^Y = n_3^Z = \hat{\mathbf{n}} \cdot \hat{\boldsymbol{\nu}} \neq 0 \,. \tag{11}$$

The last inequality above follows from the assumption that the central image ray hits the reflector. As such, the vectors $\hat{\mathbf{n}}$ and $\hat{\boldsymbol{\nu}}$ cannot be perpendicular. In accordance with Červený (2001), we let $\mathbf{G}$ denote the 2×2 upper left sub-matrix of matrix $\hat{\mathbf{G}}$. Moreover, we adopt the form of matrix $\hat{\mathbf{G}}$ used by Iversen (2005),

$$\hat{\mathbf{G}} = \begin{pmatrix} \mathbf{G} & \mathbf{n}^Z \\ \boldsymbol{\nu}^{YT} & G_{33} \end{pmatrix} \,, \tag{12}$$

where the two-component vector, $\boldsymbol{\nu}^Y$, is the projection of the full reflector normal, $\hat{\boldsymbol{\nu}}^Y$, onto the $\mathbf{y}$-plane, and $G_{33} = n_3^Z = \nu_3^Y$. Setting

$$\mathbf{f} = -\frac{\boldsymbol{\nu}^Y}{\nu_3^Y}, \quad \text{with} \quad \nu_3^Y = \pm \frac{1}{\sqrt{1 + \mathbf{f}^T \mathbf{f}}} \,, \tag{13}$$

the reflector normal can be given as

$$\hat{\boldsymbol{\nu}}^Y = \nu_3^Y \begin{pmatrix} -\mathbf{f} \\ 1 \end{pmatrix} \,. \tag{14}$$

Note that a convention for the vector direction must be specified. By selecting "+" or "-" the reflector normal will be pointing in the same or opposite direction to that of the image-ray slowness vector, that means, down and up, respectively.

Using equation 10 one can also express the reflector dip in wavefront-orthonormal coordinates as

$$\mathbf{f} = \mathbf{G}^{-1} \mathbf{n}^Z = c\, \mathbf{G}^{-1} \mathbf{p}^Z \,. \tag{15}$$

Determination of matrix G

It is instructive to say a few words on the determination of matrix $\mathbf{G}$ and we start by recalling that the vector $\hat{\boldsymbol{\nu}}^Y$ coincides with the y_3-axis of the $\hat{\mathbf{y}}$-system. The specification of the two remaining (y_1, y_2)-axes can be constructed according to any preferred convention, as long as to make up a right-handed Cartesian system. Note especially that it is not necessary to require the local reflector coordinate system to be aligned with the plane of incidence. Once the $\hat{\mathbf{z}}$-system is chosen, the corresponding transformation matrix, $\hat{\mathbf{G}}$, is readily computed. A simple choice for the coordinate axis $(\hat{\mathbf{z}}_1, \hat{\mathbf{z}}_2, \hat{\mathbf{z}}_3)$ of the $\hat{\mathbf{z}}$-system is to set $\hat{\mathbf{z}}_3 = \hat{\boldsymbol{\nu}}$ and to define the remaining axes as

$$\hat{\mathbf{z}}_1 = \frac{\hat{\mathbf{y}}_2 \times \hat{\boldsymbol{\nu}}}{|\hat{\mathbf{y}}_2 \times \hat{\boldsymbol{\nu}}|} \quad \text{and} \quad \hat{\mathbf{z}}_2 = \hat{\boldsymbol{\nu}} \times \hat{\mathbf{z}}_1 \ . \tag{16}$$

The above definitions yield

$$\hat{\mathbf{G}} = \begin{pmatrix} \hat{\mathbf{z}}_1^Y & \hat{\mathbf{z}}_2^Y & \hat{\mathbf{z}}_3^Y \end{pmatrix}^T = \begin{pmatrix} \dfrac{\nu_3^Y}{a} & 0 & -\dfrac{\nu_1^Y}{a} \\[2mm] -\dfrac{\nu_1^Y \nu_2^Y}{a} & a & -\dfrac{\nu_2^Y \nu_3^Y}{a} \\[2mm] \nu_1^Y & \nu_2^Y & \nu_3^Y \end{pmatrix} \ , \quad \text{with} \quad a = \sqrt{\nu_1^{Y\,2} + \nu_3^{Y\,2}} \ . \tag{17}$$

Note, in particular, that if $\hat{\boldsymbol{\nu}}$ is parallel to $\hat{\mathbf{z}}_3$, the transformation matrix reduces to the identity matrix, $\hat{\mathbf{G}} = \hat{\mathbf{I}}$.

SURFACE-TO-SURFACE PROPAGATOR MATRIX

For various purposes, it is convenient to introduce the 4×4 surface-to-surface propagator matrix of the one-way central (downgoing) image ray

$$\mathcal{T} = \begin{pmatrix} \mathcal{A} & \mathcal{B} \\ \mathcal{C} & \mathcal{D} \end{pmatrix} \ , \tag{18}$$

which connects the (known) measurement surface $\mathcal{M}$ to the (unknown) target reflector, $\mathcal{Z}$. Detailed descriptions and applications of the surface-to-surface propagator matrix concept can be found in, e.g., Bortfeld (1989), Červený (2001) and Schleicher et al. (2007).

As shown in (Iversen, 2006), the wavefront coordinate system allows for the computation of the submatrix systems $(\mathbf{Q}_E, \mathbf{P}_E)$ and $(\mathbf{Q}_D, \mathbf{P}_D)$, which correspond to hypothetical wavefront solutions initialized in the same point as an "exploding" measurement surface (E) and a point diffractor (D). The two solutions form the 4×4 matrix

$$\mathbf{\Phi} = \begin{pmatrix} \mathbf{Q}_E & \mathbf{Q}_D \\ \mathbf{P}_E & \mathbf{P}_D \end{pmatrix} , \tag{19}$$

which constitutes the surface-to-surface propagator matrix of the central image ray with respect to the given measurement surface and the wavefront surface that corresponds to the central image ray at the IIP. We remark that the above-defined propagator matrix is an inherent property of the given central image ray and measurement surface, defined independently of the reflector.

The introduction of the $\hat{\mathbf{y}}$-system enables the decomposition of the propagator matrix in the form

$$\mathbf{\mathcal{T}} = \mathbf{Y}\mathbf{\Phi} , \tag{20}$$

where $\mathbf{Y}$ is the so-called *projection matrix*, which embodies the properties of the reflector and provides the link between the propagator matrices $\mathbf{\mathcal{T}}$ and $\mathbf{\Phi}$. With the help of the matrix $\hat{\mathbf{G}}$, we can obtain an explicit expression of the projection matrix, $\mathbf{Y}$, included in equation 20. It is given by (Červený, 2001)

$$\mathbf{Y} = \begin{pmatrix} (\mathbf{G} - \mathbf{A}^{an})^{-T} & \mathbf{0} \\ \left(\mathbf{E} - p_3^Z \mathbf{D}\right) (\mathbf{G} - \mathbf{A}^{an})^{-T} & (\mathbf{G} - \mathbf{A}^{an}) \end{pmatrix} . \tag{21}$$

The 2×2 matrix $\mathbf{E}$, referred to as the *inhomogeneity matrix*, is given by

$$E_{IJ} = \frac{1}{c} \left[G_{I3} G_{JM} \, \eta_M^Y + G_{J3} G_{IK} \, \eta_K^Y + G_{I3} G_{J3} (\eta_3^Y - \frac{1}{c} \eta_L^Y v_L^Y) \right] , \qquad (22)$$

while

$$\mathbf{A}^{an} \equiv \mathbf{p}^Z \mathbf{v}^{YT} \qquad (23)$$

is the 2×2 *anisotropy matrix*. The entities $v_i{}^Y$ and $\eta_i{}^Y$, $i = 1, 2, 3$, are components of the ray-velocity vector $\hat{\mathbf{v}}^Y$ and the "eta vector" $d\hat{\mathbf{p}}^Y/dt$ (derivative of slowness vector with respect to traveltime), specified in wavefront-orthonormal coordinates. For isotropic media, we have $\mathbf{A}^{an} = \mathbf{0}$. It is to be observed that in many situations, one can also consider that $\mathbf{E} = \mathbf{0}$. For example, this is the case if the medium is locally homogeneous. The matrix $\mathbf{E}$ is also zero if the slowness vector is normal to the reflector.

Inserting the projection matrix equation 21 into the decomposition equation 20, the propagator matrix components can be recast as

$$\mathcal{A} = (\mathbf{G} - \mathbf{A}^{an})^{-T} \mathbf{Q}_E , \qquad (24)$$

$$\mathcal{C} = \left(\mathbf{E} - p_3^Z \mathbf{D} \right) \mathcal{A} + \mathcal{A}^{-T} \mathbf{Q}_E{}^T \mathbf{P}_E , \qquad (25)$$

and similarly

$$\mathcal{B} = (\mathbf{G} - \mathbf{A}^{an})^{-T} \mathbf{Q}_D , \qquad (26)$$

$$\mathcal{D} = \left(\mathbf{E} - p_3^Z \mathbf{D} \right) \mathcal{B} + \mathcal{B}^{-T} \mathbf{Q}_D{}^T \mathbf{P}_D . \qquad (27)$$

EXPRESSIONS FOR REFLECTOR DIP AND CURVATURE

The one-way traveltime along image rays from the measurement surface to the reflector is denoted here as $\mathcal{T}(\mathbf{m})$. In Appendix A we have derived two fundamental equations for the first and second derivatives of the function $\mathcal{T}$. These relations are used in the following

to obtain expressions for dip and curvature of the reflector. The key relationship in this context is the condition

$$T^M(\mathbf{m}) = 2\mathcal{T}(\mathbf{m}) \ , \tag{28}$$

which we differentiate twice with respect to coordinates m_K and evaluate at $\mathbf{m} = \mathbf{0}$.

Expression for reflector dip

The reflector dip $\mathbf{f}$, in wavefront-orthonormal coordinates, has to satisfy equation 15 derived above. Moreover, by applying the condition 28 to the fundamental relation A-14 involving the surface-to surface traveltime gradient we obtain

$$\mathbf{p}^Z = \frac{1}{2}\mathcal{A}^{-T}\mathbf{p}^M \ , \tag{29}$$

where $\mathbf{p}^M = \partial T^M/\partial \mathbf{m}$ is assumed known. We shall also need equations 23 and 24 specifying, respectively, the anisotropy matrix $\mathbf{A}^{an}$ and the projection matrix $\mathcal{A}$. Combining all this yields the result

$$\mathbf{f} = \frac{c}{2}\left(1 + \kappa\right)^{-1}\mathbf{Q}_E^{-T}\mathbf{p}^M \ , \tag{30}$$

where the scalar κ has the definition

$$\kappa = \frac{1}{2}\mathbf{v}^{YT}\mathbf{Q}_E^{-T}\mathbf{p}^M \ . \tag{31}$$

If the medium is isotropic at the final point of the central ray, we have $\kappa = 0$.

Taken into account equations 13 and 14, the sought-for reflector unit normal, $\hat{\boldsymbol{\nu}}$, is obtained. The transformation matrix $\hat{\mathbf{G}}$ can also be computed, e.g., using equation 17. Knowing $\hat{\mathbf{G}}$ we can obtain matrices $\mathbf{E}$, $\mathbf{A}^{an}$, and $\mathcal{A}$, which are needed for estimation of reflector curvature.

Expression for reflector curvature

In the following we use equations A-23 and A-24 from Appendix A which connects the curvature matrix to second derivatives of surface-to-surface traveltime. Taking into account the condition 28, we obtain

$$\frac{1}{2}\mathbf{M}^M \;=\; \boldsymbol{\mathcal{A}}^T\boldsymbol{\mathcal{C}}_0 - \frac{1}{v_3^Z}\,\boldsymbol{\mathcal{A}}^T\mathbf{D}\boldsymbol{\mathcal{A}}\;, \tag{32}$$

where, as indicated in Appendix A, matrix $\boldsymbol{\mathcal{C}}_0$ is computed by substituting $\mathbf{D} = \mathbf{0}$ in equation 25. Minor rearranging of equation 32 then yields

$$\mathbf{D} = v_3^Z\left(\boldsymbol{\mathcal{C}}_0\boldsymbol{\mathcal{A}}^{-1} - \frac{1}{2}\boldsymbol{\mathcal{A}}^{-T}\mathbf{M}^M\boldsymbol{\mathcal{A}}^{-1}\right)\;. \tag{33}$$

It may be desirable to express v_3^Z in terms of the scalar κ defined in equation 31. This yields

$$\mathbf{D} = \frac{c\,n_3^Z}{1+\kappa}\left(\boldsymbol{\mathcal{C}}_0\boldsymbol{\mathcal{A}}^{-1} - \frac{1}{2}\boldsymbol{\mathcal{A}}^{-T}\mathbf{M}^M\boldsymbol{\mathcal{A}}^{-1}\right)\;. \tag{34}$$

The equivalent equations 33 and 34 provide the sought-for reflector curvature, thus completing the solution of our problem. The knowledge of dip and curvature quantities permit us to obtain the complete surface-to-surface propagator matrix of the central image ray, as specified above by equations 24 - 27.

NUMERICAL EXAMPLES

In this section we present two numerical examples of mapping traveltime parameters belonging to the migrated time domain to corresponding parameters in the depth domain, using a known macro-velocity depth model. Observe that depth-domain coordinates are from now on referred to as (x, y, z).

Experiment 1: 2-D anisotropic model

Consider a cylindrical reflector situated in a smooth 2-D anisotropic medium (Figure 6). The anisotropy is of type TTI (tilted transversely isotropic) with a fixed symmetry axis in the direction specified by the vector $(u_x, u_y, u_z) = (0.1, 0, 1)$ [unit]. The P-wave velocity along this axis is given by the linear function $V_P(x, z) = 2.28 + 0.02x + 0.2z$ [km/s], while the corresponding S-wave velocities are computed using Poisson's ratio so that $V_S(x, z) = V_P(x, z)/\sqrt{3}$. Thomsen's parameters ϵ and δ have the values 0.2 and 0.1, respectively. The cylindrical reflector has its axis in the y-direction and a radius of 1 km. The axis passes through the reference point (0, 0, 2.5) [km].

To obtain synthetic measurements we traced image rays from the measurement surface until they hit the cylinder. One can observe (Figure 6) that the resulting ray trajectories are not perpendicular to the measurement surface. Computed ray traveltimes were multiplied by two and used for generation of a cubic B-spline function. From this function we obtained "measured" input parameters (times, slopes, and second derivatives) to be used for estimation of reflector depths, dips, and curvatures.

Figure 7 compares analytic values of reflector depth, dip, and curvature to corresponding estimated values obtained using the true velocity model in the time-to-depth mapping procedure. The theoretical results are confirmed through this example, but it is important to remark that the curvature estimation is particularly exposed to small numerical errors as well as to measurement errors. Therefore, to obtain reliable results in "real" situations it will be critical to perform appropriate smoothing of the input time parameters. We also did a time-to-depth mapping test where anisotropy was ignored in the velocity model (Figure 8). One can then observe a significant mispositioning of the estimated reflector and

corresponding systematic errors in estimated dip and curvature.

Experiment 2: 3-D isotropic model

A 3-D isotropic model (Figure 9) containing planar and curved non-intersecting interfaces was chosen as the "true" model for the experiment. By tracing image rays in this layered model, we obtained reflection time maps in the migrated domain, one such map for each model interface.

Although input reflection time maps were obtained using the layered model in Figure 9, it is more natural for the image-ray time-to-depth mapping to use a velocity grid, as is common in time and depth migration. Appropriate smoothing of this depth velocity field is a must. Here we used smoothing in the form of a repeated processing by a Hamming operator, applied independently to the various coordinate directions. This Hamming-operator smoothing is constrained by a certain aperture or radius, defined as the maximum distance within which a given data sample contributes to the smoothing of neighboring samples. For the model under consideration, the Hamming radius was set to 0.8 km.

Results of the time-to-depth mapping procedure are presented here for one single reflector, namely, the one with depths ranging between 2.97 and 3.27 km. The input reflection time parameters for this selected reflector are shown in Figures 10 through 15. The six input parameters are the reflection time, the slopes in the x and y directions, the main second derivatives (xx and yy), and finally the mixed second derivative (xy). In Figures 16 through 21 we compare parameters of the true depth reflector to those estimated by the time-to-depth mapping procedure. The parameters are the reflection depth, the reflector dips (x and y), and the associated second derivatives (xx, yy, xy).

The mean error in the estimated depth of the selected reflector is 9 m. This is to be compared to the mean depth of the reflector, which is 3152 m. Furthermore, comparison of the true and estimated first and second derivatives shows a high degree of consistency, thus indicating that the method has a good potential for success in practice, when applying a sufficiently smooth depth velocity model. We remark that more smoothing is required to obtain consistent dips than consistent depths, and even more smoothing is required to obtain consistent second derivatives.

CONCLUSIONS

Considering symmetric primary-reflected waves, the geological dip and curvature of a target reflector can be expressed in terms of the traveltime and its first and second derivatives in the time-migrated domain. The obtained expressions extend previous results in the literature to fully anisotropic and inhomogeneous layered media. In addition, the formulation uses the elegant machinery of surface-to-surface propagator matrices, making the derivations more simple and transparent. Potential application of the obtained results can be, for example, the construction of selected reflectors in depth to help setting constraints for velocity-model building. Smoothing of the velocity field and the measured input parameters is of ultimate importance, especially concerning estimation of reflector curvature. Synthetic examples confirm the theoretical results and are encouraging for further testing and realistic applications.

ACKNOWLEDGMENTS

APPENDIX A

SURFACE-TO-SURFACE TRAVELTIME RELATIONS FOR THE IMAGE-RAY FIELD

In this appendix we derive general transformations relations pertaining to an exploding-surface ray field, i.e., a ray field where individual rays are started simultaneously at a given initial (anterior) surface. The slowness vectors of the rays are normal to this surface. The rays are captured on a final (anterior) surface. The image-ray field is a special case of such exploding-surface ray fields. The anterior surface is then the measurement surface (datum surface) in the time-migrated domain, while the posterior surface is the target reflector.

We denote the standard ray coordinates for the image-ray field as $\hat{\boldsymbol{\gamma}} = (\mathbf{m}, t)$. Here, t is the traveltime from the exploding measurement surface, $\mathcal{M}$. On the surface $\mathcal{M}$ itself we therefore have $t = 0$. In the following, we let the measurement surface be planar and the coordinates $\mathbf{m}$ be Cartesian such that $\mathbf{m} = \mathbf{0}$ for a certain central ray. However, this does not imply loss of generality, as the derived relations are valid also when $\mathbf{m} = (m_1, m_2)$ is defined as orthogonal curvilinear coordinates for a generally shaped measurement surface. Moreover, in the following we take advantage of an alternative ray coordinate system for the exploding-surface ray field, described by the vector $\hat{\boldsymbol{\mu}} = (\mathbf{m}, t^{\mathcal{Z}})$. Here the parameter

$t^{\mathcal{Z}}$ is the traveltime measured from the reflector surface $\mathcal{Z}$. Along the surface $\mathcal{Z}$ we have $t^{\mathcal{Z}} = 0$.

The traveltime parameters t and $t^{\mathcal{Z}}$ are independent variables. However, for a point on a given ray, specified by the vector $\mathbf{m}$, we can connect the two parameters via the relation

$$t^{\mathcal{Z}} = t - \mathcal{T} \ , \tag{A-1}$$

where $\mathcal{T}$ denotes the surface-to-surface traveltime.

General properties

Let S be an arbitrary differentiable variable which can be either a function of the ray coordinates $\hat{\boldsymbol{\mu}}$ or the local Cartesian reflector coordinates $\hat{\mathbf{z}}$. The chain rule for derivatives then yields

$$\frac{\partial S}{\partial \mu_i} = \frac{\partial S}{\partial z_m} \frac{\partial z_m}{\partial \mu_i} \ . \tag{A-2}$$

In particular, if $S = \mu_k$, one obtains the well-known relation between the forward transformation matrix $(\partial z_m / \partial \mu_i)$ and its inverse $(\partial \mu_k / \partial z_m)$,

$$\frac{\partial \mu_k}{\partial z_m} \frac{\partial z_m}{\partial \mu_i} = \delta_{ki} \ . \tag{A-3}$$

We make the following observations:

- The partial derivatives $\partial z_M / \partial m_I$ are taken for constant $t^{\mathcal{Z}}$. When $t^{\mathcal{Z}} = 0$ we can identify these derivatives as the elements of 2×2 submatrix $\boldsymbol{A}$ of the 4×4 surface-to-surface propagator matrix, i.e.,

$$\mathcal{A}_{MI} = \frac{\partial z_M}{\partial m_I} \ . \tag{A-4}$$

- The first partial derivatives of z_3 with respect to m_I are also taken for constant $t^{\mathcal{Z}}$.

  When $\mathbf{m} = \mathbf{0}$ and $t^{\mathcal{Z}} = 0$ we have

$$\frac{\partial z_3}{\partial m_I} = 0 \ . \tag{A-5}$$

  To derive the above result, we observe that, if $t^{\mathcal{Z}} = 0$, points are on the reflector, namely $z_3 = \Sigma(\mathbf{z})$. As a consequence, keeping $t^{\mathcal{Z}} = 0$, we have

$$\frac{\partial z_3}{\partial m_I} = \frac{\partial \Sigma}{\partial z_M} \frac{\partial z_M}{\partial m_I} \ . \tag{A-6}$$

  Equation A-5 now follows, since $\mathbf{z} = \mathbf{0}$ when $\mathbf{m} = \mathbf{0}$ and $t^{\mathcal{Z}} = 0$ and also $(\partial \Sigma / \partial z_M)(\mathbf{0}) = 0$, we have $\mathbf{z} = \mathbf{0}$,

- Partial differentiation with respect to t and $t^{\mathcal{Z}}$ is equivalent, since $\mathbf{m}$ is kept constant in both situations. Therefore, we have

$$\frac{\partial z_M}{\partial t^{\mathcal{Z}}} = \frac{\partial z_M}{\partial t} = v_M^Z \ , \qquad \frac{\partial z_3}{\partial t^{\mathcal{Z}}} = \frac{\partial z_3}{\partial t} = v_3^Z \ . \tag{A-7}$$

- Considering only differentiation with respect to the first two components $\mu_I = m_I$ of $\hat{\boldsymbol{\mu}}$ in equation A-2 one can write

$$\frac{\partial S}{\partial m_I} = \frac{\partial S}{\partial z_M} \frac{\partial z_M}{\partial m_I} + \frac{\partial S}{\partial z_3} \frac{\partial z_3}{\partial m_I} \ . \tag{A-8}$$

  Differentiation with respect to $\mathbf{m}$ in equation A-8 is, by definition, performed for constant $t^{\mathcal{Z}}$. If $\mathbf{m} = \mathbf{0}$ and $t^{\mathcal{Z}} = 0$ we use equation A-5 to obtain

$$\frac{\partial S}{\partial m_I} = \frac{\partial S}{\partial z_M} \frac{\partial z_M}{\partial m_I} \ . \tag{A-9}$$

- The situation $k = 3$ in equation A-3 is described specifically by the equations

$$\frac{\partial t^{\mathcal{Z}}}{\partial z_M} \frac{\partial z_M}{\partial m_I} + \frac{\partial t^{\mathcal{Z}}}{\partial z_3} \frac{\partial z_3}{\partial m_I} = 0 \ , \qquad \frac{\partial t^{\mathcal{Z}}}{\partial z_M} \frac{\partial z_M}{\partial t^{\mathcal{Z}}} + \frac{\partial t^{\mathcal{Z}}}{\partial z_3} \frac{\partial z_3}{\partial t^{\mathcal{Z}}} = 1 \ . \tag{A-10}$$

  Using equations A-5 and A-7 for $\mathbf{m} = \mathbf{0}$ and $t^{\mathcal{Z}} = 0$ then gives

$$\frac{\partial t^{\mathcal{Z}}}{\partial z_I} = 0 \ , \qquad \frac{\partial t^{\mathcal{Z}}}{\partial z_3} = \frac{1}{v_3^Z} \ . \tag{A-11}$$

Surface-to-surface traveltime relation: first order

Differentiating equation A-1 with respect to $\mathbf{z}$ yields

$$\frac{\partial t^{\mathcal{Z}}}{\partial z_M} = \frac{\partial t}{\partial z_M} - \frac{\partial \mathcal{T}}{\partial z_M} \;, \qquad \frac{\partial t^{\mathcal{Z}}}{\partial \mathbf{z}} = \frac{\partial t}{\partial \mathbf{z}} - \frac{\partial \mathcal{T}}{\partial \mathbf{z}} \;. \tag{A-12}$$

Using $S = \mathcal{T}$ in equation A-9,

$$\frac{\partial \mathcal{T}}{\partial m_I} = \frac{\partial z_M}{\partial m_I} \frac{\partial \mathcal{T}}{\partial z_M} \;, \qquad \frac{\partial \mathcal{T}}{\partial \mathbf{m}} = \mathcal{A}^T \frac{\partial \mathcal{T}}{\partial \mathbf{z}} \;, \tag{A-13}$$

and the fact that $\partial t^{\mathcal{Z}}/\partial \mathbf{z} = \mathbf{0}$ then shows that the vector form of equation A-12 can be restated as

$$\frac{\partial t}{\partial \mathbf{z}} = \mathcal{A}^{-T} \frac{\partial \mathcal{T}}{\partial \mathbf{m}} \;. \tag{A-14}$$

Equation A-14 is a fundamental equation that can be used to relate the dip of the reflector to the gradient, $\partial \mathcal{T}/\partial \mathbf{m}$, of surface-to-surface traveltime. The vector $\partial t/\partial \mathbf{z}$ contains the first two components of the slowness vector at the IIP. This slowness vector projection belongs to the local Cartesian $(\mathbf{z}, z_3)$ coordinate system and is equivalently referred to as

$$\mathbf{p}^Z = \frac{\partial t}{\partial \mathbf{z}} \;. \tag{A-15}$$

Surface-to-surface traveltime relation: second order

We differentiate the leftmost equation A-10 with respect to components m_J as follows,

$$\frac{\partial}{\partial m_J} \left(\frac{\partial t^{\mathcal{Z}}}{\partial z_M} \frac{\partial z_M}{\partial m_I} + \frac{\partial t^{\mathcal{Z}}}{\partial z_3} \frac{\partial z_3}{\partial m_I} \right) = 0 \;. \tag{A-16}$$

Working out the various terms yields

$$\frac{\partial z_M}{\partial m_I} \frac{\partial}{\partial m_J} \left(\frac{\partial t^{\mathcal{Z}}}{\partial z_M} \right) + \frac{\partial t^{\mathcal{Z}}}{\partial z_3} \frac{\partial^2 z_3}{\partial m_I \partial m_J} + \ldots = 0 \;, \tag{A-17}$$

where the dots $(\ldots)$ signify terms that contain partial derivatives of the type $\partial z_3/\partial m_I$ or $\partial t^{\mathcal{Z}}/\partial z_M$. For $\mathbf{m} = \mathbf{0}$ and $t^{\mathcal{Z}} = 0$ all such terms are zero. We now apply equation

A-1 in equation A-17 and insert the surface function $z_3 = \Sigma^{\mathcal{Z}}(\mathbf{z})$. Elaboration equation A-17 further utilizing the general differential operator in equation A-8, and finally requiring $\mathbf{m} = \mathbf{0}$ and $t^{\mathcal{Z}} = 0$, we obtain

$$\frac{\partial^2 \mathcal{T}}{\partial m_I \partial m_J} = \frac{\partial z_M}{\partial m_I} \left(\frac{\partial^2 t}{\partial z_M \partial z_N} + \frac{\partial t^{\mathcal{Z}}}{\partial z_3} \frac{\partial^2 \Sigma^{\mathcal{Z}}}{\partial z_M \partial z_N} \right) \frac{\partial z_N}{\partial m_J} \ . \tag{A-18}$$

In the above derivations, we have made use of the results

$$\frac{\partial z_M}{\partial m_I} \frac{\partial}{\partial m_J} \left(\frac{\partial t}{\partial z_M} \right) = \frac{\partial z_M}{\partial m_I} \frac{\partial^2 t}{\partial z_M \partial z_N} \frac{\partial z_N}{\partial m_J} \ , \tag{A-19}$$

and

$$\frac{\partial z_M}{\partial m_I} \frac{\partial}{\partial m_J} \left(\frac{\partial \mathcal{T}}{\partial z_M} \right) = \frac{\partial z_M}{\partial m_I} \frac{\partial}{\partial z_M} \left(\frac{\partial \mathcal{T}}{\partial m_J} \right) = \frac{\partial^2 \mathcal{T}}{\partial m_I \partial m_J} \ , \tag{A-20}$$

as well as the properties 6 of the reflector. Using the rightmost equation A-11 and also the definition of the reflector curvature matrix

$$D_{MN} = -\frac{\partial^2 \Sigma^{\mathcal{Z}}}{\partial z_M \partial z_N} \ , \tag{A-21}$$

also given by equation 6, our final result in component form appears as

$$\frac{\partial^2 \mathcal{T}}{\partial m_I \partial m_J} = \frac{\partial z_M}{\partial m_I} \left(\frac{\partial^2 t}{\partial z_M \partial z_N} - \frac{1}{v_3^Z} D_{MN} \right) \frac{\partial z_N}{\partial m_J} \ . \tag{A-22}$$

The corresponding matrix form of equation A-22 is

$$\frac{\partial^2 \mathcal{T}}{\partial \mathbf{m}^2} = \boldsymbol{\mathcal{A}}^T \left(\frac{\partial^2 t}{\partial \mathbf{z}^2} - \frac{1}{v_3^Z} \mathbf{D} \right) \boldsymbol{\mathcal{A}} \ . \tag{A-23}$$

Equation A-23 is a fundamental relation that relates the curvature matrix, $\mathbf{D}$, of the reflector to the second derivatives of the surface-to-surface traveltime, $\partial^2 \mathcal{T} / \partial \mathbf{m}^2$.

The matrix $\partial^2 t / \partial \mathbf{z}^2$ contains second derivatives of the traveltime from the measurement surface taken along the tangent plane of the reflector. We can therefore compute this matrix as

$$\frac{\partial^2 t}{\partial \mathbf{z}^2} = \boldsymbol{\mathcal{C}}_0 \boldsymbol{\mathcal{A}}^{-1} \ , \tag{A-24}$$

where matrix $\mathcal{C}_0$ is a special version of the submatrix $\mathbf{C}$ contained within the surface-to-surface propagator matrix $\mathcal{T}$: matrix $\mathcal{C}_0$ corresponds to evaluating matrix $\mathcal{C}$ with zero reflector curvatures.

REFERENCES

Bilette, F. and G. Lambaré, 1998, Velocity macro-model estimation from seismic reflsection data by stereotomography: Geophysical Journal International, **135**, 671–690.

Biloti, R., L. T. Santos, and M. Tygel, 2002, Multiparametric traveltime inversion: Studia Geophysica et Geodaetica, **46**, 177–192.

Bortfeld, R., 1989, Geometrical ray theory: Rays and traveltimes in seismic systems (second-order approximation of the traveltimes): Geophysics, **54**, 342–349.

Cameron, M. K., S. Fomel, and J. A. Sethian, 2006, Seismic velocity estimation and time to depth conversion of time-migrated images, *in* 76th Ann. Internat. Mtg., SEG, Expanded Abstracts, 3066–3070.

———, 2007, Seismic velocity estimation from time migration: Inverse Problems, **23**, 1329–1369.

———, 2008, Time-to-depth conversion and seismic velocity estimation using time-migration velocity: Geophysics, **73**, VE205–VE210.

Červený, V., 2001, Seismic ray theory. Cambridge University Press.

Claerbout, J. F., 1992, Earth soundings analysis: Processing versus inversion. Blackwell Scientific Publications, Inc.

Duveneck, E., 2004, Velocity model estimation with data-derived wavefront attributes: Geophysics, **69**, 265–274.

Fomel, S., 2002, Application of plane-wave destruction filters: Geophysics, **67**, 1946–1960.

———, 2007, Application of plane-wave destruction filters: Geophysics, **72**, S139–S147.

Gjøystdal, H. and B. Ursin, 1981, Inversion of reflection times in three-dimensions: Geophysics, **46**, 972–983.

Hertweck, T., C. Jäger, J. Mann, E. Duveneck, and Z. Heilmann, 2004, A seismic reflec-

tion imaging workflow based on the common-relection-surface (crs) stack: Theoretical background and case study, *in* 74th Ann. Internat. Mtg., SEG, Expanded Abstracts, 2032–2035.

Hubral, P., 1977, Time migration - Some ray theoretical aspects: Geophysical Prospecting, **25**, 738–745.

———, 1983, Computing true-amplitude reflections in a laterally inhomogeneous earth: Geophysics, **48**, 1051–1062.

Hubral, P. and T. Krey, 1980, Interval Velocities from Seismic Reflection Time Measurements, Soc. of Expl. Geophys.

Iversen, E., 2005, Tangent vectors of isochron rays and velocity rays expressed in global Cartesian coordinates: Studia Geophysica et Geodaetica, **49**, 525–540.

———, 2006, Amplitude, Fresnel zone, and NMO velocity for PP and SS normal-incidence reflections: Geophysics, **71**, W1–W14.

Iversen, E., K. Åstebøl, and H. Gjøystdal, 1987, Time-to-depth conversion of 3D seismic interpretation data by use of 'dynamic image rays', *in* 49th Ann. Internat. Mtg., Eur. Ass. of Expl. Geophys., Expanded Abstracts, 16.

———, 1988, 3D time-to-depth conversion of interpreted time-migrated horizons by use of the paraxial image ray method: Research report, NORSAR, Norway.

Iversen, E. and H. Gjøystdal, 1984, Three-dimensional velocity inversion by use of kinematic and dynamic ray tracing, *in* 54th Ann. Internat. Mtg., SEG, Expanded Abstracts, 643–645.

Iversen, E. and M. Tygel, 2008, Image-ray tracing for joint 3D seismic velocity estimation and time-to-depth conversion: Geophysics, **73**, P99–P114.

Kleyn, A. H., 1977, On the migration of reflection time contour maps: Geophysical prospect-

ing, **25**, 125–140.

Landa, E., B. Gurevich, S. Keydar, and P. Trachtman, 1999, Application of multifocus for subsuface imaging: Applied Geophysics, **42**, 263–300.

Robein, E., 2003, Velocities, time-imaging and depth-imaging in reflection seismics. Principles and methods, Eur. Ass. of Expl. Geophys.

Schleicher, J., M. Tygel, and P. Hubral, 2007, Seismic true-amplitude imaging. Society of Exploration Geophysicists.

Tygel, M. and L. T. Santos, 2007, Quadratic normal moveouts of symmetric reflections in elastic media: a quick tutorial: Studia Geophysica et Geodaetica, **51**, 185–206.

Ursin, B., 1982, Time-to-depth migration using wavefront curvature: Geophysical Prospecting, **30**, 261–280.

Yilmaz, O., 2000, Seismic data analysis vol. 1. Soc. of Expl. Geophys.

LIST OF FIGURES
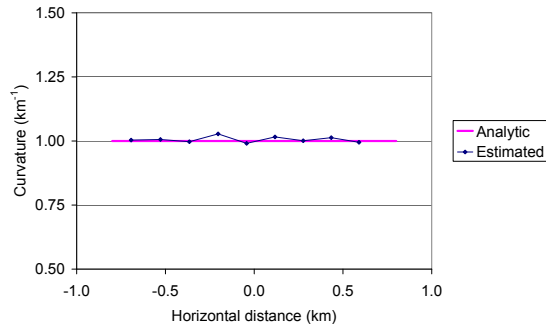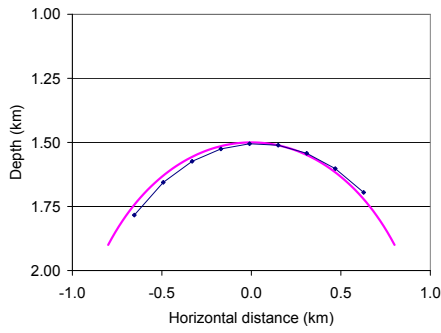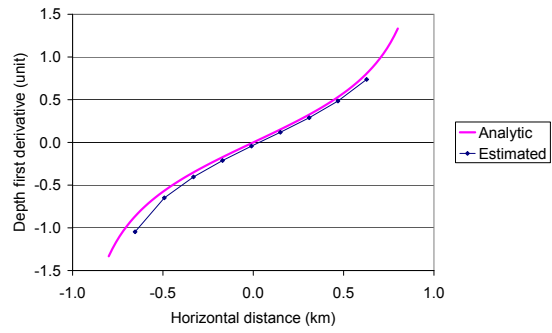
8   Analytic and estimated values of (a) depths, (b) dips, and (c) curvatures for the cylindrical reflector shown in Figure 6. Anisotropy was ignored in the image-ray time-to-depth mapping.
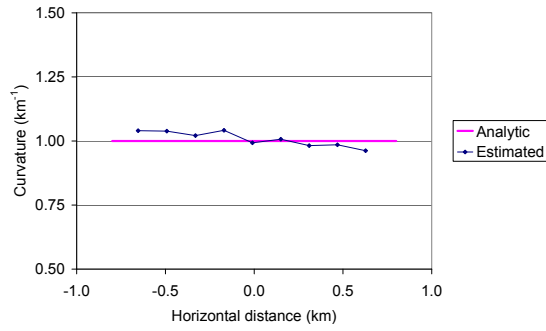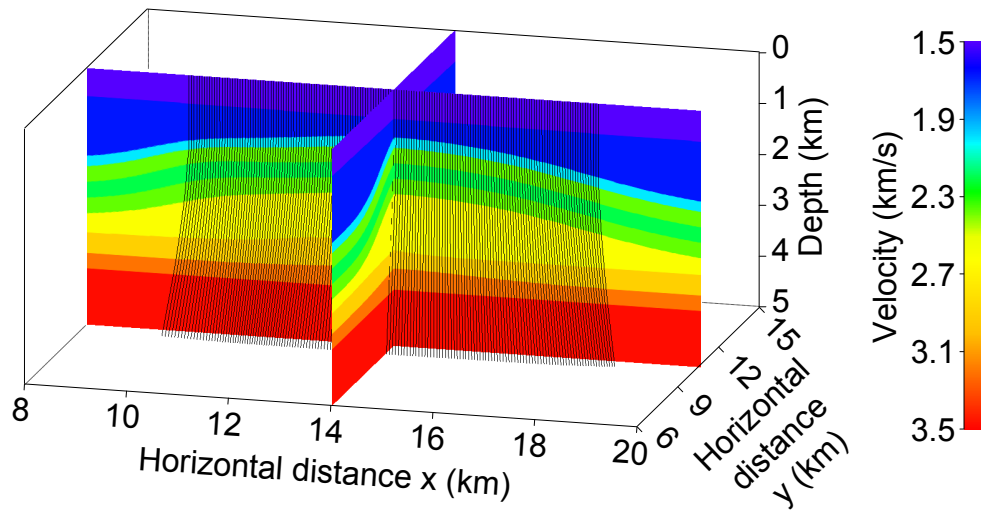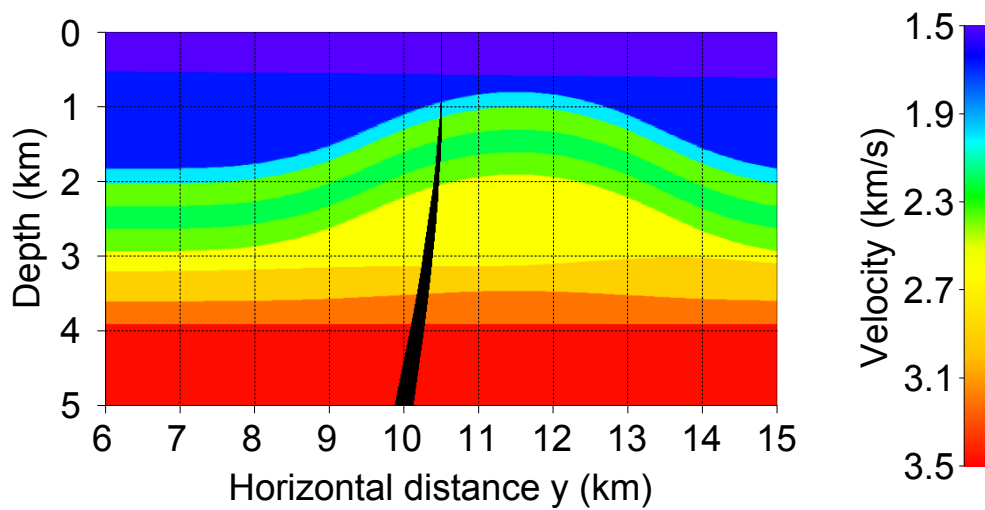
9   Experiment 2: (a) 3-D view of image ray trajectories starting along the line $y = 10.5$ (km) in the measurement surface, (b) projection of the same trajectories into the cross section $x = 14$ (km).

10   Simulated migrated time horizon corresponding to the selected depth reflector. The depths of this reflector are confined between 2.97 and 3.27 km.

11   Slope x of the simulated migrated time horizon.

12   Slope y of the simulated migrated time horizon.

13   Second derivative xx of the simulated migrated time horizon.

14   Second derivative yy of the simulated migrated time horizon.

15   Second derivative xy of the simulated migrated time horizon.

16   Depth (a) of the true depth reflector and (b) estimated by the image-ray time-to-depth mapping method.

17   Dip x (a) of the true depth reflector and (b) estimated by the image-ray time-to-depth mapping method.

18   Dip y (a) of the true depth reflector and (b) estimated by the image-ray time-to-depth mapping method.

19   Second derivative xx (a) of the true depth reflector and (b) estimated by the image-ray time-to-depth mapping method.

20   Second derivative yy (a) of the true depth reflector and (b) estimated by the image-ray time-to-depth mapping method.

21   Second derivative xy (a) of the true depth reflector and (b) estimated by the image-

ray time-to-depth mapping method.
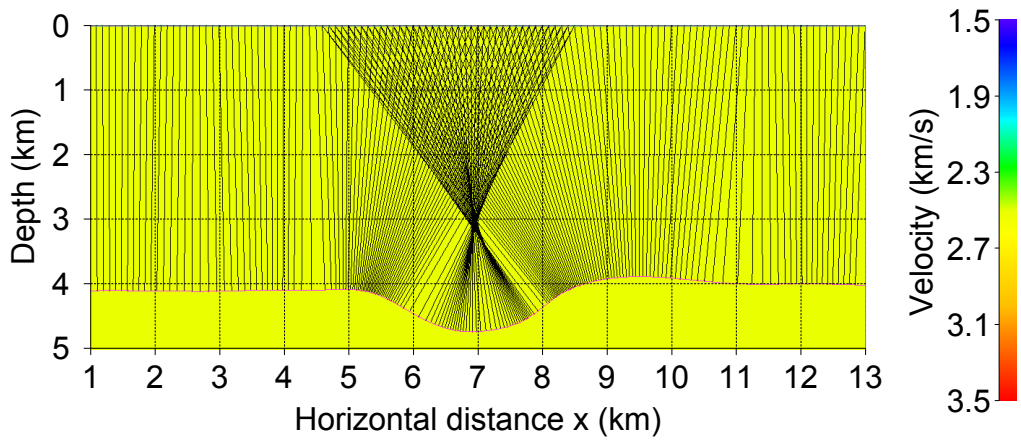
(a)
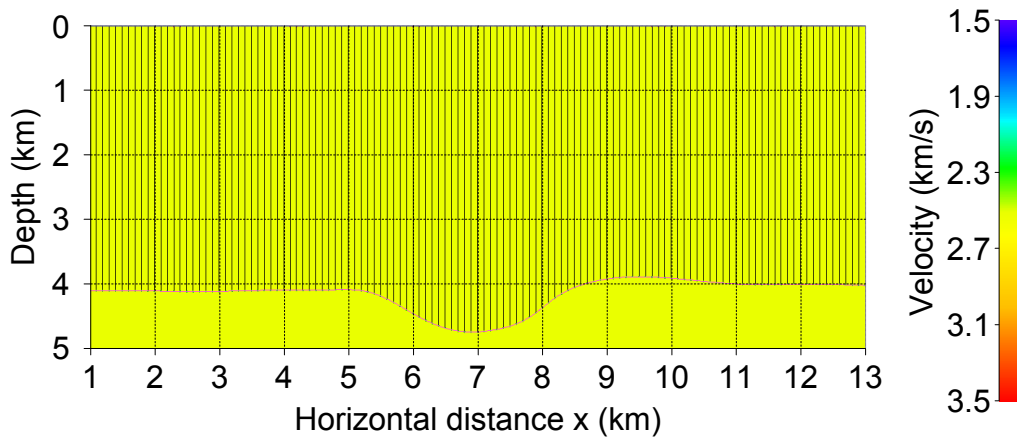
(b)

Figure 1: (a) Normal-ray and (b) image-ray trajectories for a syncline-shaped reflector in a homogeneous isotropic velocity field. The measurement surface is a horizontal plane. The normal-ray field is sampled regularly at the measurement surface; the image-ray field is sampled regularly at the reflector.

Tygel & Ursin & Iversen & de Hoop –
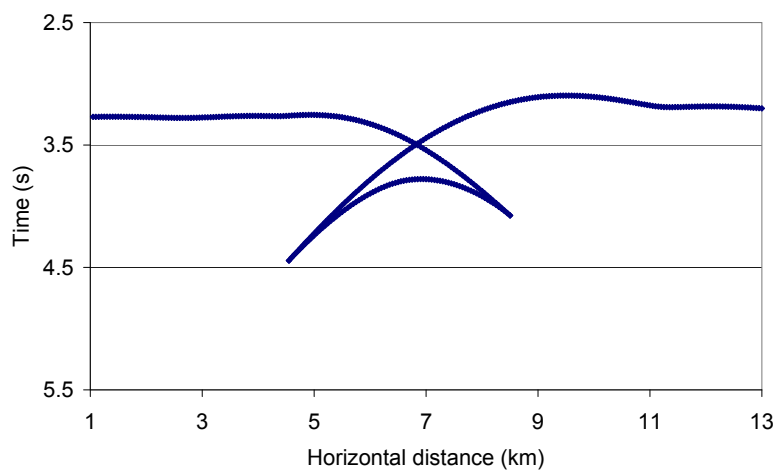
(a)
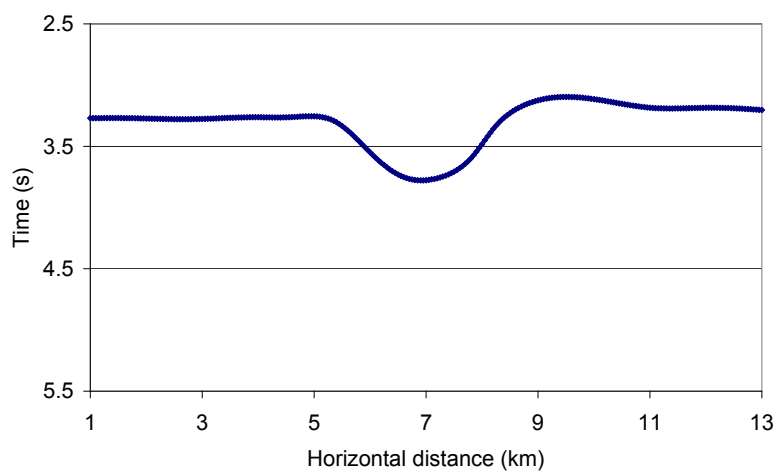
(b)

Figure 2: Two-way times, in (a) the unmigrated domain and (b) the migrated domain, corresponding to the ray fields shown in Figure 1.

Tygel & Ursin & Iversen & de Hoop –
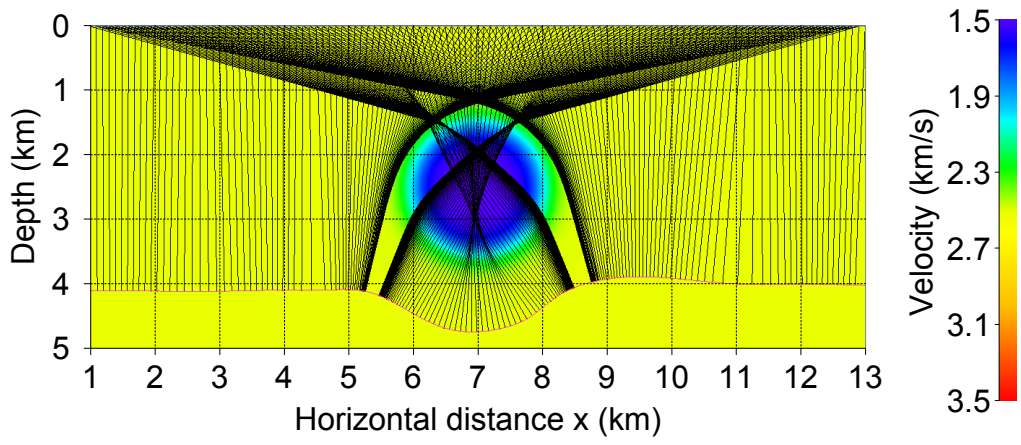
(a)
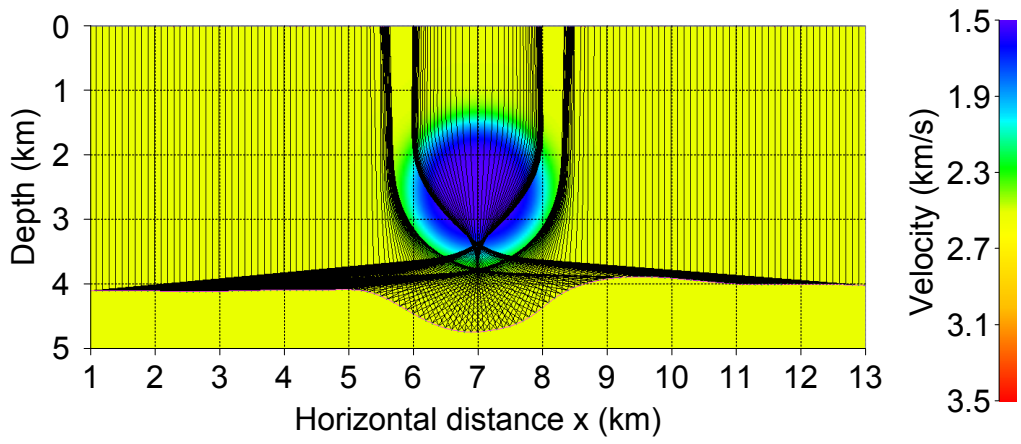
(b)

Figure 3: (a) Normal-ray and (b) image-ray trajectories in the presence of a low-velocity inclusion. The measurement and reflector surfaces are identical to those in Figure 1. The normal-ray field is sampled regularly at the measurement surface; the image-ray field is sampled regularly at the reflector.

Tygel & Ursin & Iversen & de Hoop –
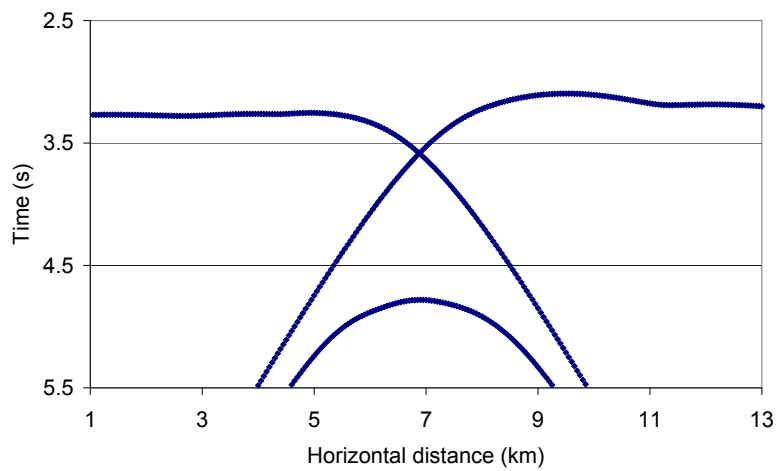
(a)
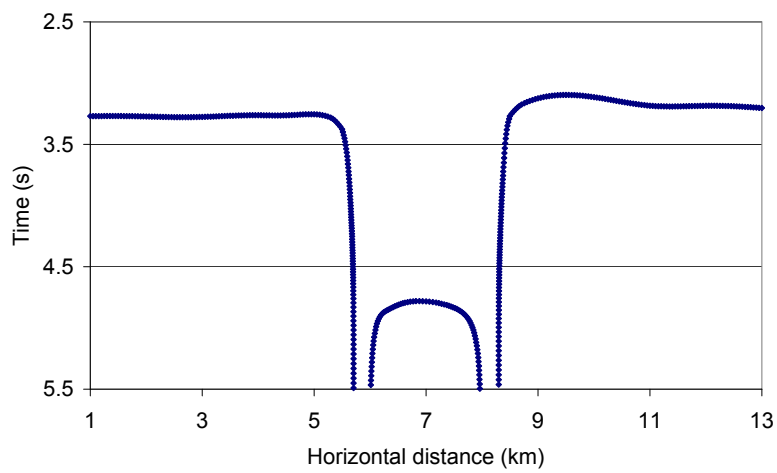
(b)

Figure 4: Two-way times, in (a) the unmigrated domain and (b) the migrated domain, corresponding to the ray fields shown in Figure 3.

Tygel & Ursin & Iversen & de Hoop –
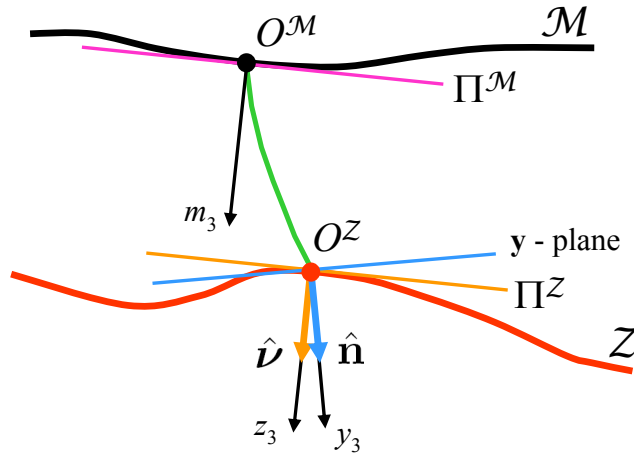
(a)
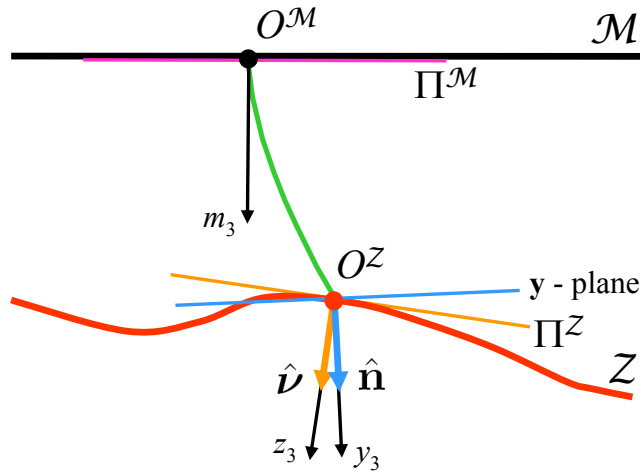
(b)

Figure 5: Time-migration measurement (datum) surface $\mathcal{M}$ (black), reflector $\mathcal{Z}$ (red), image ray (green) and associated quantities defined in the text: tangent planes, local Cartesian coordinate systems, and unit normals, $\hat{\mathbf{n}}$ and $\hat{\boldsymbol{\nu}}$ to wavefront and reflector, respectively. (a) General scenario including a curved measurement surface (b) Planar and horizontal measurement surface commonly used for time migration.

39
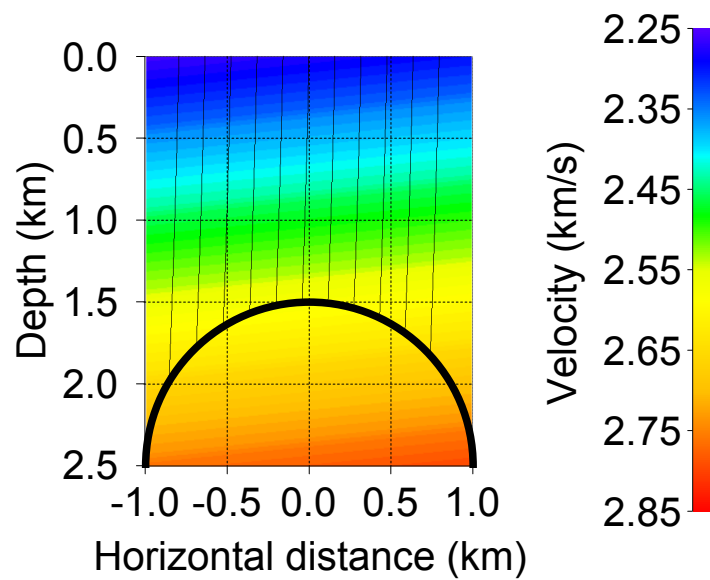
Figure 6: Experiment 1: Cylindrical reflector situated in an inhomogeneous tilted transversely isotropic medium. Image ray trajectories used for generation of "observed" two-way times in the migrated domain are superimposed.

Tygel & Ursin & Iversen & de Hoop –
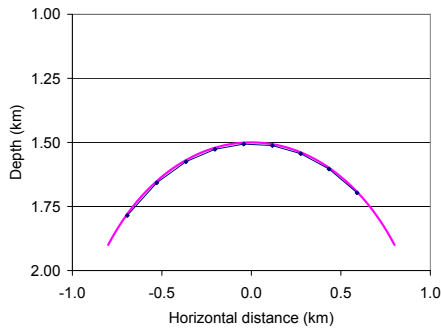
(a)
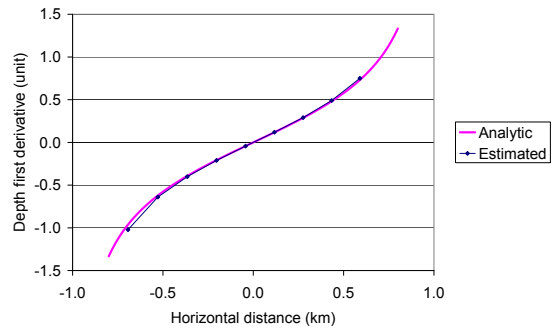
(b)

(c)

Figure 7: Analytic and estimated values of (a) depths, (b) dips, and (c) curvatures for the cylindrical reflector shown in Figure 6. The true anisotropic velocity model was used for image-ray time-to-depth mapping.

Tygel & Ursin & Iversen & de Hoop –

(a)

(b)

(c)

Figure 8: Analytic and estimated values of (a) depths, (b) dips, and (c) curvatures for the cylindrical reflector shown in Figure 6. Anisotropy was ignored in the image-ray time-to-depth mapping.

Tygel & Ursin & Iversen & de Hoop –

(a)

(b)

Figure 9: Experiment 2: (a) 3-D view of image ray trajectories starting along the line $y = 10.5$ (km) in the measurement surface, (b) projection of the same trajectories into the cross section $x = 14$ (km).
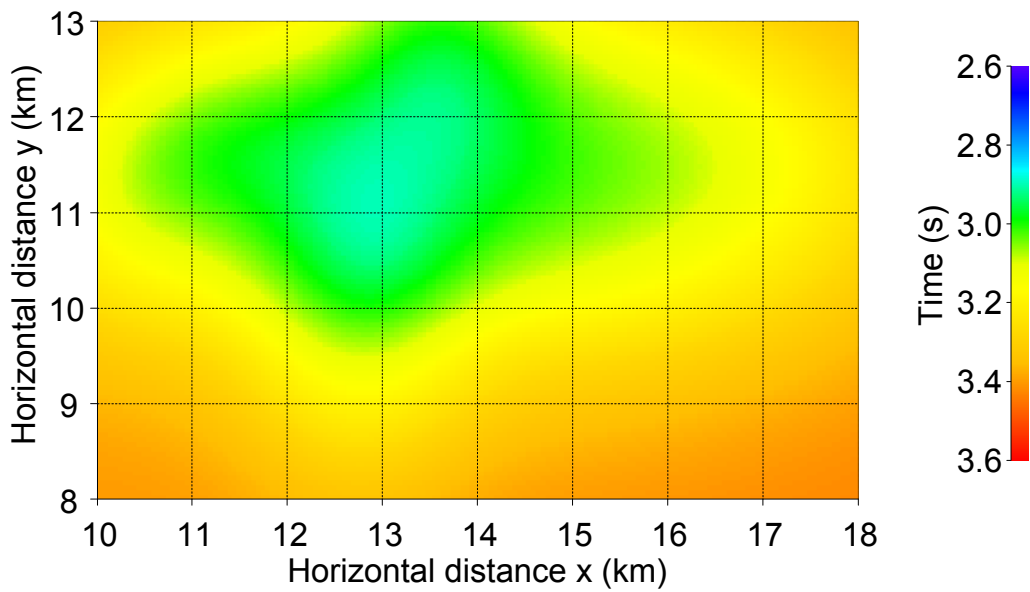
Figure 10: Simulated migrated time horizon corresponding to the selected depth reflector.

The depths of this reflector are confined between 2.97 and 3.27 km.

Tygel & Ursin & Iversen & de Hoop –
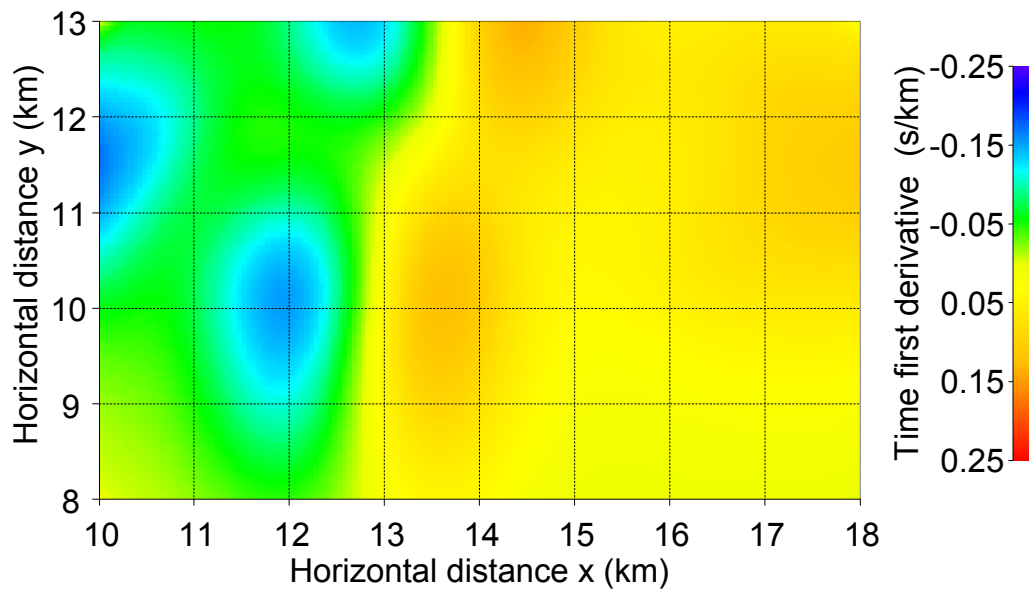
Figure 11: Slope x of the simulated migrated time horizon.

Tygel & Ursin & Iversen & de Hoop –
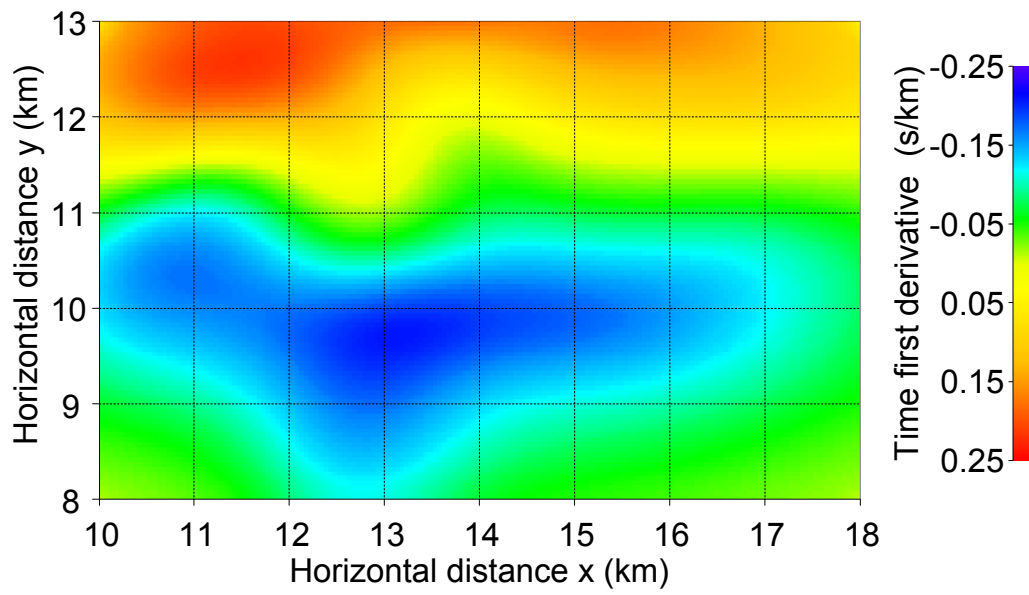
Figure 12: Slope y of the simulated migrated time horizon.

Tygel & Ursin & Iversen & de Hoop –
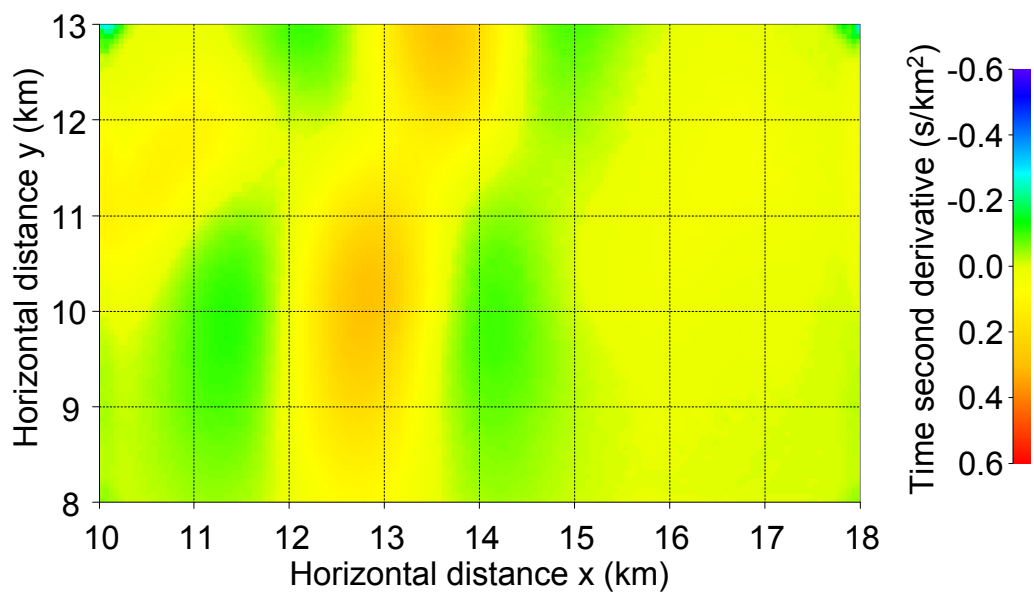
Figure 13: Second derivative xx of the simulated migrated time horizon.

Tygel & Ursin & Iversen & de Hoop –
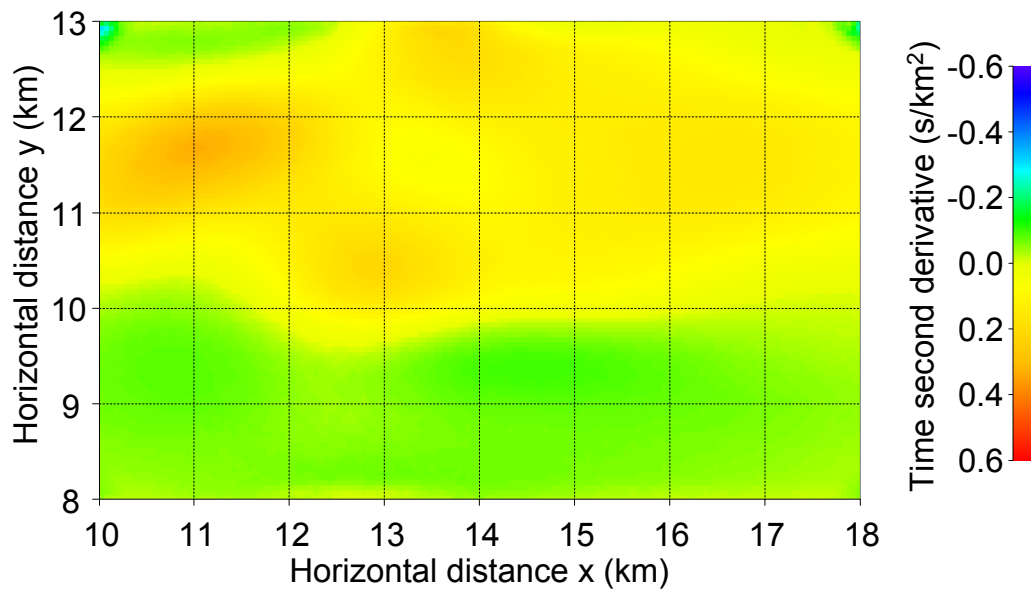
Figure 14: Second derivative yy of the simulated migrated time horizon.

Tygel & Ursin & Iversen & de Hoop –
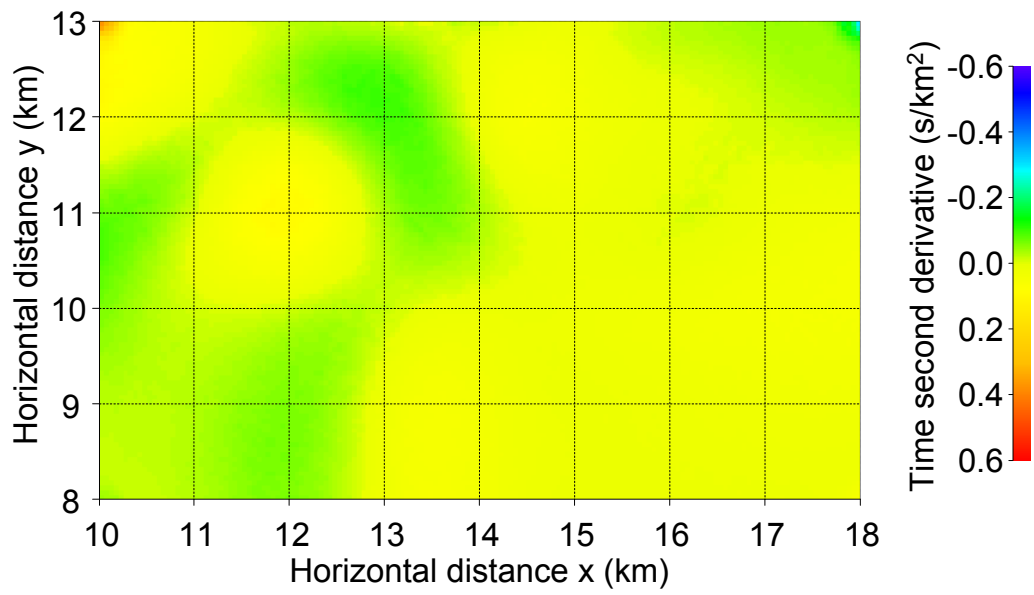
Figure 15: Second derivative xy of the simulated migrated time horizon.
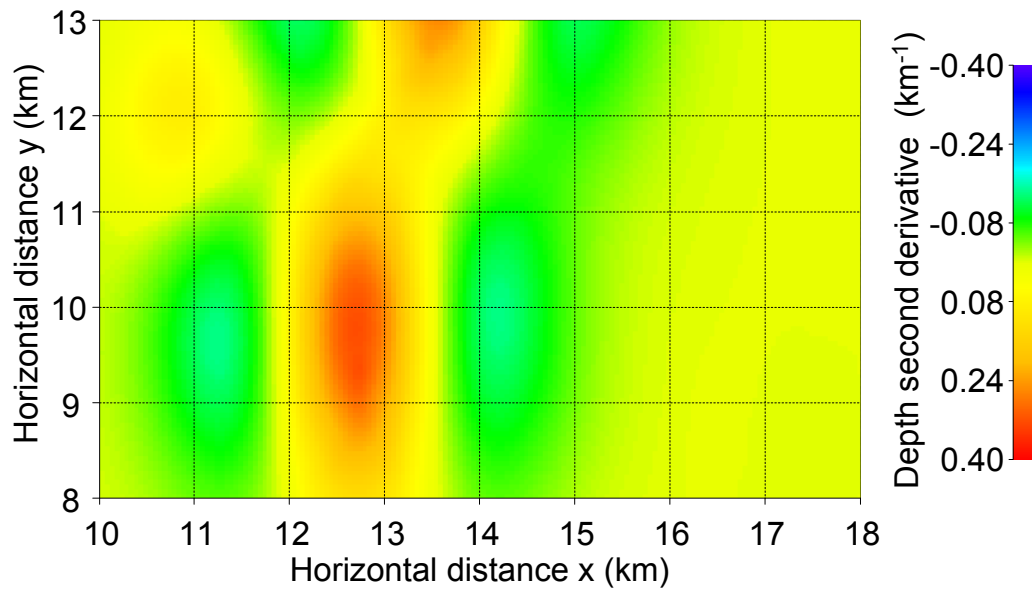
Tygel & Ursin & Iversen & de Hoop –

(a)

(b)

Figure 16: Depth (a) of the true depth reflector and (b) estimated by the image-ray time-to-depth mapping method.

50

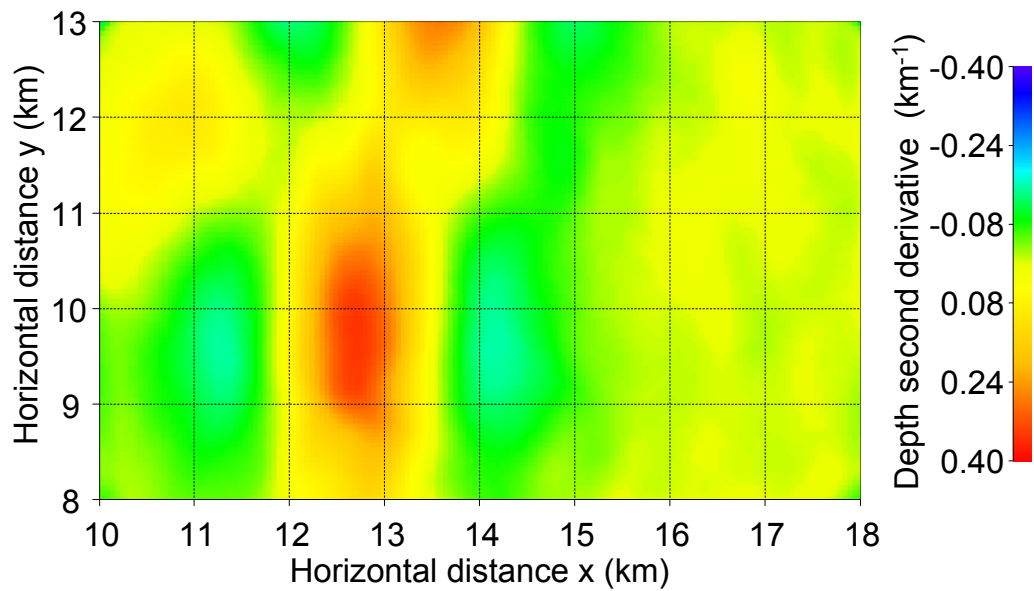**Tygel & Ursin & Iversen & de Hoop** –
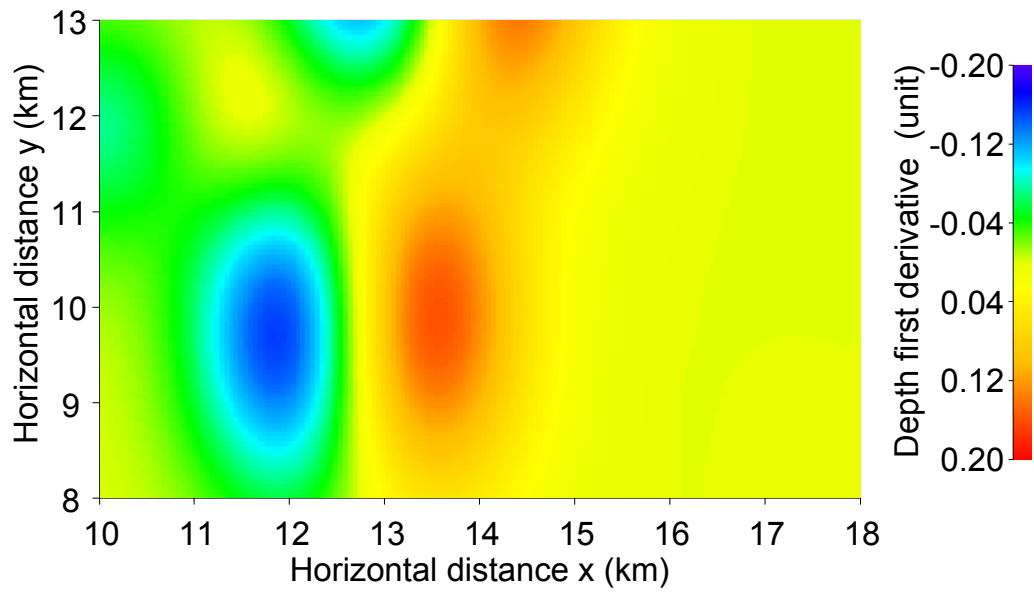
(a)
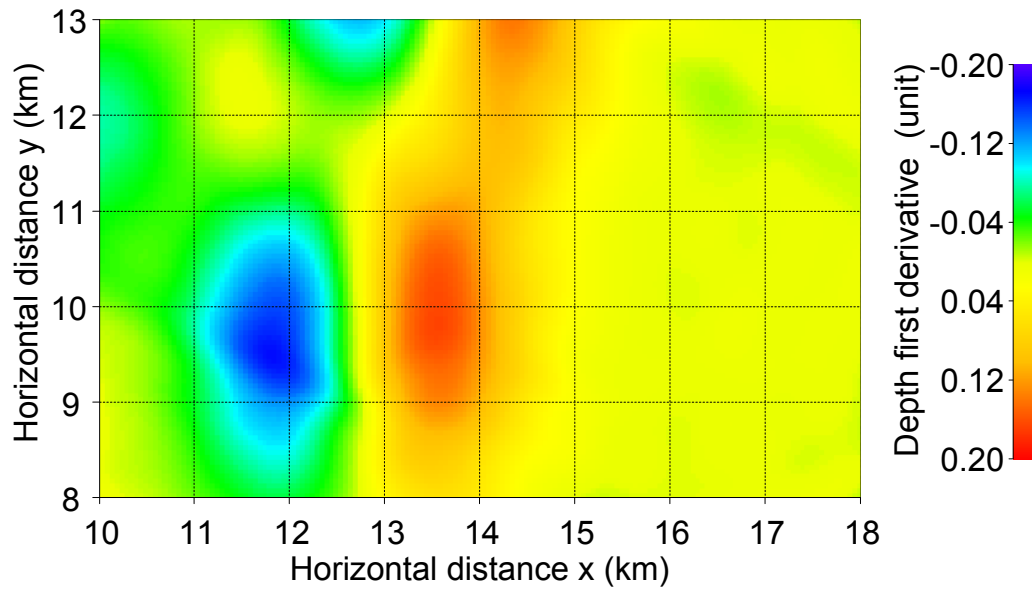
(b)

Figure 17: Dip x (a) of the true depth reflector and (b) estimated by the image-ray time-to-depth mapping method.

Tygel & Ursin & Iversen & de Hoop –
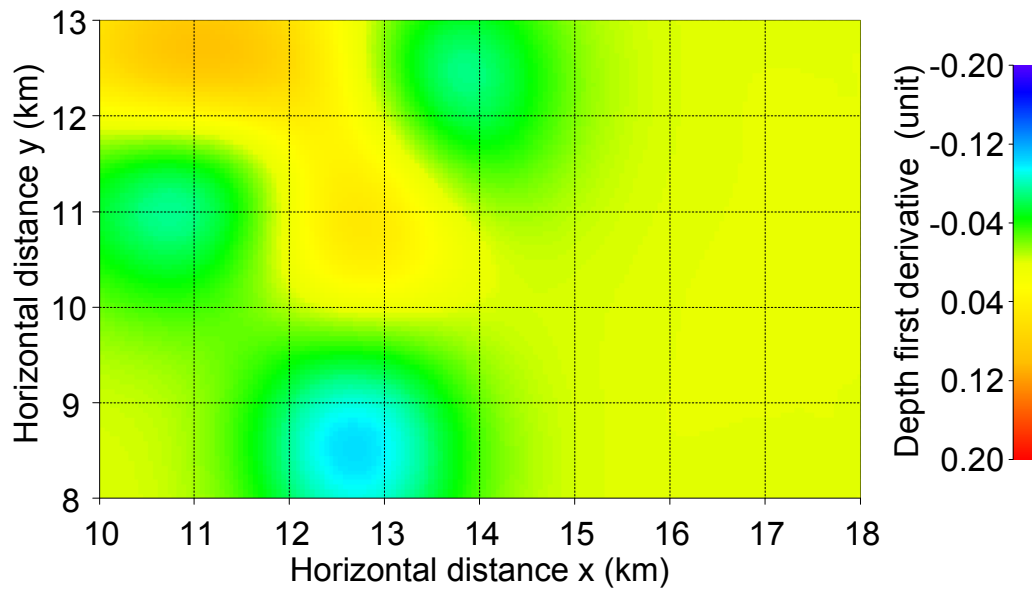
(a)
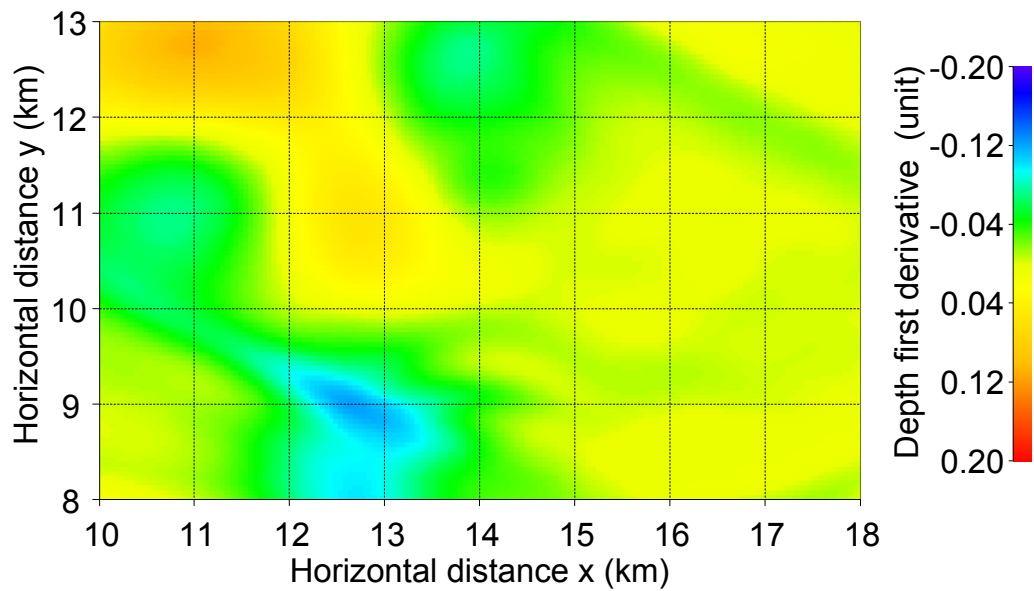
(b)

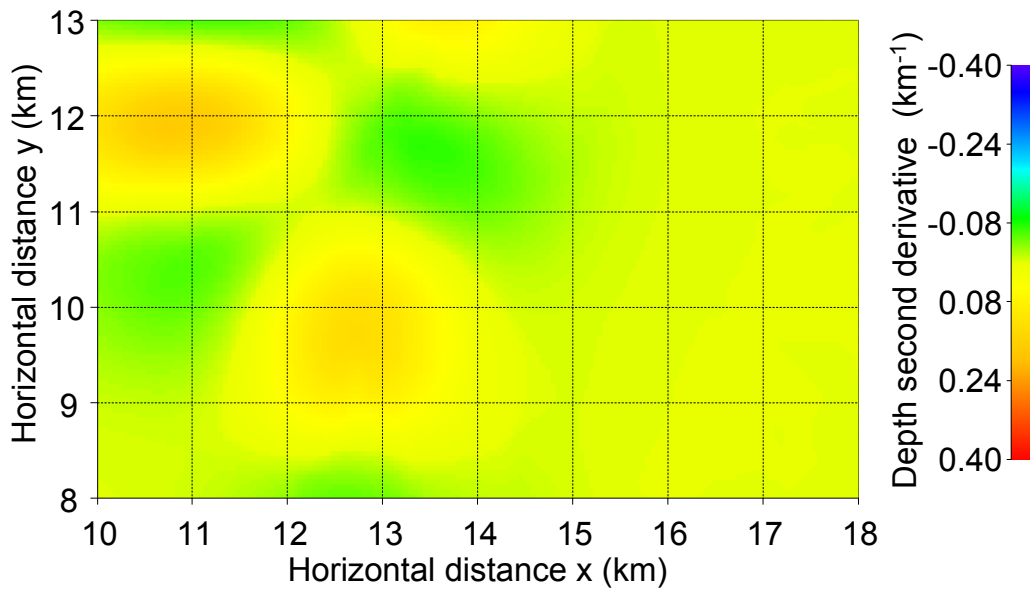Figure 18: Dip y (a) of the true depth reflector and (b) estimated by the image-ray time-to-depth mapping method.

Tygel & Ursin & Iversen & de Hoop –

(a)
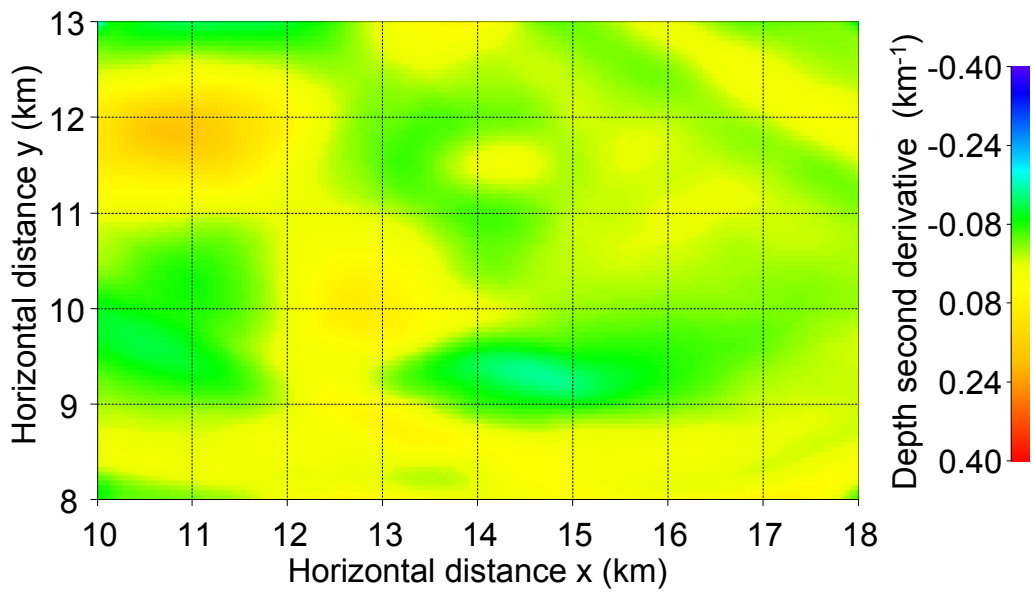

(b)

Figure 19: Second derivative xx (a) of the true depth reflector and (b) estimated by the image-ray time-to-depth mapping method.

53

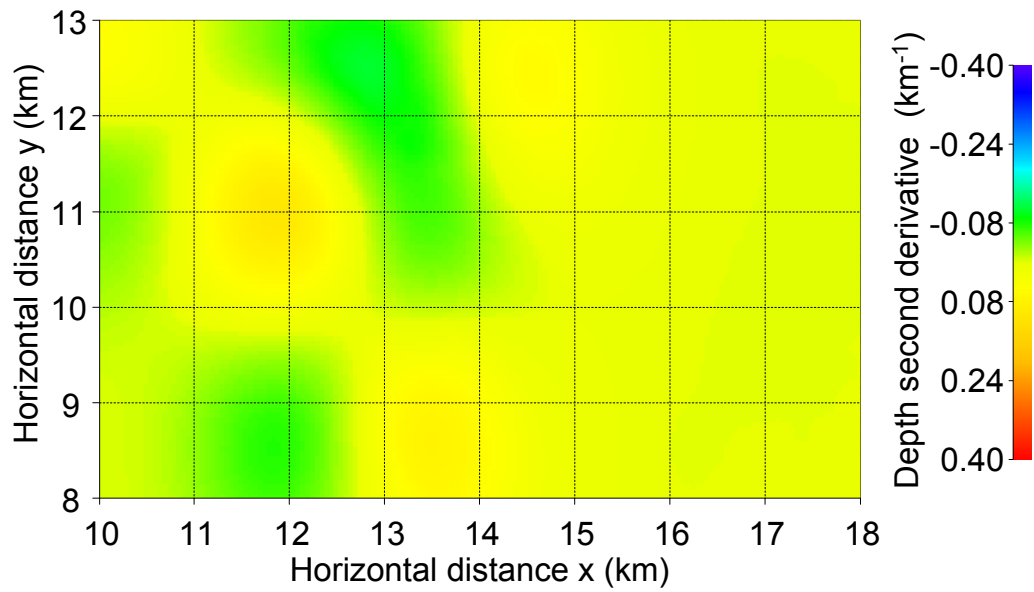**Tygel & Ursin & Iversen & de Hoop** –
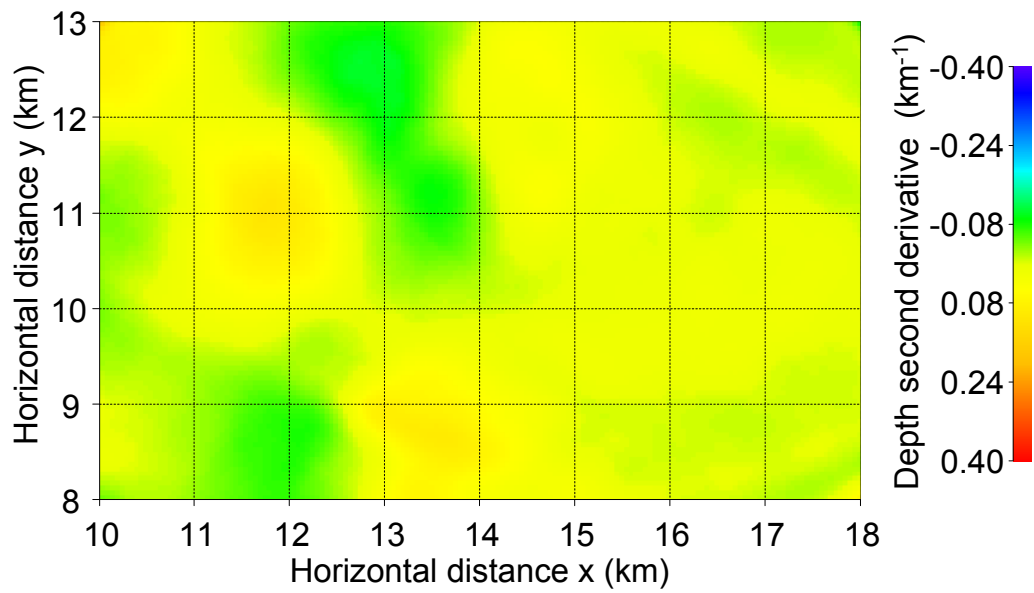
(a)

(b)

Figure 20: Second derivative yy (a) of the true depth reflector and (b) estimated by the image-ray time-to-depth mapping method.

54

(a)

(b)

Figure 21: Second derivative xy (a) of the true depth reflector and (b) estimated by the image-ray time-to-depth mapping method.

Tygel & Ursin & Iversen & de Hoop –